Molecular Therapy
Methods & Clinical Development
Original Article

High-titer AAV disrupts cerebrovascular integrity and induces lymphocyte infiltration in adult mouse brain

Yaowei Guo,[1] Junliang Chen,[1] Wenyu Ji,[1] Liang Xu,[1] Yu Xie,[1] Shu He,[1] Chuying Lai,[1] Kaiyu Hou,[1] Zeru Li,[1] Gong Chen,[1] and Zheng Wu[1]

[1]Key Laboratory of CNS Regeneration (Ministry of Education), Guangdong Key Laboratory of Non-human Primate Research, GHM Institute of CNS Regeneration, Jinan University, Guangzhou 510632, China

The brain is often described as an "immune-privileged" organ due to the presence of the blood-brain-barrier (BBB), which limits the entry of immune cells. In general, intracranial injection of adeno-associated virus (AAV) is considered a relatively safe procedure. In this study, we discovered that AAV, a popular engineered viral vector for gene therapy, can disrupt the BBB and induce immune cell infiltration in a titer-dependent manner. First, our bulk RNA sequencing data revealed that injection of high-titer AAV significantly upregulated many genes involved in disrupting BBB integrity and antiviral adaptive immune responses. By using histologic analysis, we further demonstrated that the biological structure of the BBB was severely disrupted in the adult mouse brain. Meanwhile, we noticed abnormal leakage of blood components, including immune cells, within the brain parenchyma of high-titer AAV injected areas. Moreover, we identified that the majority of infiltrated immune cells were cytotoxic T lymphocytes (CTLs), which resulted in a massive loss of neurons at the site of AAV injection. In addition, antagonizing CTL function by administering antibodies significantly reduced neuronal toxicity induced by high-titer AAV. Collectively, our findings underscore potential severe side effects of intracranial injection of high-titer AAV, which might compromise proper data interpretation if unaware of.

INTRODUCTION

Adeno-associated virus (AAV) is a small, non-enveloped virus that is characterized by relatively low immunogenicity and pathogenicity. Therefore, AAV has become one of the most widely used vectors in both basic research applications and gene therapy.[1–3] Although recent clinical studies have achieved success with recombinant AAV (rAAV), host immune responses to capsids and transgene products have been commonly observed in many preclinical and clinical studies.[4–6] In addition, host immune response not only limits the efficiency of AAV-based gene therapy[7–9] but also can lead to serious side effects, such as hepatobiliary disease,[10,11] and even culminates in the death of patients,[12] which has raised great concerns about the biosafety of AAV-based gene therapy.

AAVs have emerged as the most popular vectors of choice for neurological diseases due to their strong tropism for astrocytes and neurons.[13–15] In general, the invasion of immune cells across the blood-brain barrier (BBB) is highly restricted, and hence our brain is considered an "immune-privileged" organ,[16,17] imposing an impression that intracranial injection of AAV does not elicit any adaptive immune response in brain parenchyma. The BBB is formed by specialized brain microvascular endothelial cells, which are tightly sealed by adhesive proteins and sheathed by pericytes and astrocytic endfeet.[18–21] This structure maintains the highly regulated central nervous system (CNS) internal milieu and protects neurons from factors present in the circulating blood. The breakdown of the BBB enables toxic blood-derived molecules, cells, and microbial agents to enter the brain parenchyma, then contributes to inflammation and immune responses, which can further activate multiple pathways of neurodegeneration.[22–24] Disruption of the BBB is a hallmark of viral infection in the CNS, and viruses known to cause BBB breakdown include HIV, rabies virus, Zika virus, and SARS-CoV-2 virus, etc.[25–28] Nevertheless, as an engineered viral vector, whether direct injection of AAV into the brain parenchyma could also affect the BBB is largely unknown. Notably, a previous study found that high-titer AAV injection resulted in the reduction of glutamine synthetase expression, an important functional and marker protein of astrocytes for regulating neurotransmitter recycle.[29] In addition, astrocytic endfeet are one of the major biological architectures of the BBB,[20] and whether AAV injection induced astrocytic dysfunction might cause even broader brain damage has not been thoroughly explored.

Received 14 April 2023; accepted 25 August 2023;
https://doi.org/10.1016/j.omtm.2023.08.021.

Correspondence: Gong Chen, Key Laboratory of CNS Regeneration (Ministry of Education), Guangdong Key Laboratory of Non-human Primate Research, GHM Institute of CNS Regeneration, Jinan University, Guangzhou 510632, China.
E-mail: gongchen@jnu.edu.cn
Correspondence: Zheng Wu, Key Laboratory of CNS Regeneration (Ministry of Education), Guangdong Key Laboratory of Non-human Primate Research, GHM Institute of CNS Regeneration, Jinan University, Guangzhou 510632, China.
E-mail: zhengwu@jnu.edu.cn

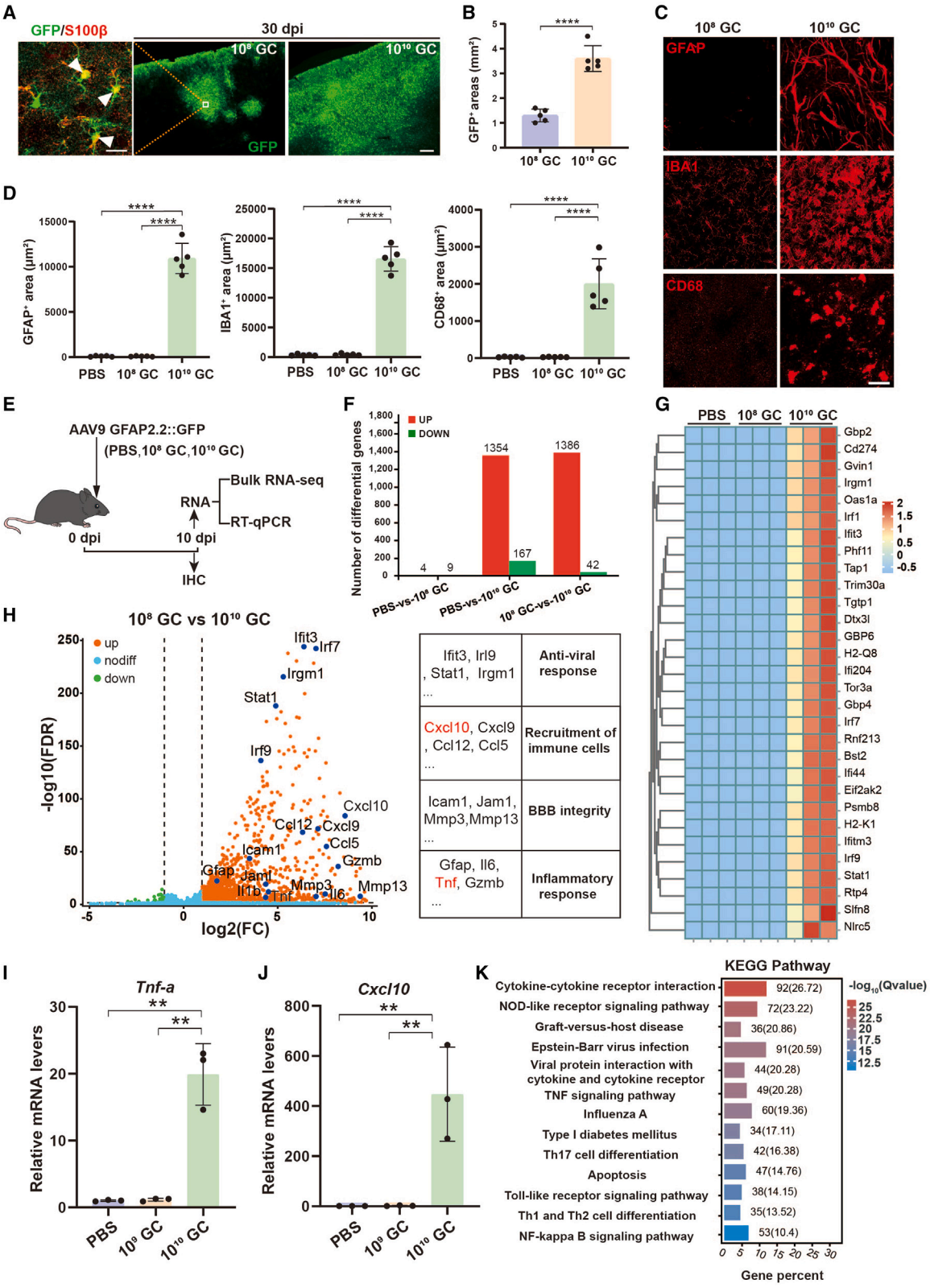

(legend on next page)

In this study, we examined changes in BBB integrity and lymphocyte infiltration following the injection of different titers of AAVs into the adult mouse brain. Using bulk RNA sequencing (RNA-seq) analysis, we found that many genes and biological processes associated with disruption of the BBB and lymphocyte infiltration were significantly upregulated in high-titer AAV treated mice. Immunostaining studies revealed that cerebrovascular cells and tight junction proteins involved in the formation of the BBB were significantly decreased after injection of high-titer AAVs. Upon BBB breakdown, leakage of plasma components, lymphocyte invasion, and neuronal damage were observed at the site of high-titer AAV injection. Further studies revealed that high-titer AAV injection induced neuronal loss is relieved by depleting infiltrated T immune cells. Taken together, our findings discover a series of detrimental effects caused by high-titer AAV injection, including cerebrovascular injury, immune cell infiltration, and neuronal toxicity.

RESULTS

AAV induces extensive changes in adaptive immune gene profiles in a titer-dependent manner

AAV vectors with cell-specific promoters are widely used for driving transgene expression in target cells, such as human glial fibrillary acidic protein promoter gfa2 (2.1 kb), which has been extensively used to induce transgene expression in astrocytes.[30,31] To validate the specificity and infected area of transgene expression in adult mouse brain, we injected AAV9-gfa2::GFP (1 μL) into the cortex at two different titers, 10^8 GC (gene copies) (low-titer, 10^{11} GC/mL) and 10^{10} GC AAV9 (high-titer, 10^{13} GC/mL), which are lower than or equal to previous studies.[32–35] Consistent with previous studies, the GFP report gene was efficiently expressed in the astrocytes (S100β$^+$) and the infected area was significantly enlarged in high-titer AAV injected mouse brains at 30 days post injection (dpi) of AAV (Figures 1A and 1B). A previous study showed that intracranial injection of high-titer AAVs affects astrocyte function (10^{10} to 3×10^{10} GC).[29] Next, we wanted to know the glial response after AAV injection, so we performed immunostaining for GFAP, Iba1, and CD68. Unexpectedly, both astrocytic marker GFAP and microglial marker Iba1 were drastically increased and many hypertrophic astrocytes and microglia were detected within the high-titer AAV injected area (Figures 1C and 1D). Moreover, the activated microglial marker CD68 was also sharply increased in high-titer AAV injected mice (Figures 1C and 1D). Together, these data suggest that high-titer AAV can induce abnormal glial responses, which may significantly change the local environment.

Next, to broadly investigate the effects of high-titer AAV on brain tissue, we performed bulk RNA-seq on the injected cortical area (1.5 mm within the injected site) from PBS (vehicle control) versus 10^8 GC and 10^{10} GC AAV9 (Figure 1E). We compared the differentially expressed genes (DEGs) (using a false discovery rate [FDR] < 0.05) between groups, and found that high-titer AAV9 injection induced a robust whole transcriptome change compared with the vehicle (DEGs = 1,521) and low-titer groups (DEGs = 1,428), while only a few DEGs were detected between PBS and low-titer groups (DEGs = 13; Figure 1F). The top 30 DEGs were presented as a heatmap according to the fold changes, which showed a significant difference between high-titer and low-titer/PBS, while there was no obvious difference between PBS and low-titer AAV (Figure 1G). Thus, to uncover the effect of high-titer AAV on the transcriptome, we further compared high-titer and low-titer AAV transcriptome datasets. A volcano plot revealed that high-titer AAV treatment enhanced more transcripts including those associated with anti-viral response (Ifit3, Irl9, Stat-1, and Irgm1), recruitment of immune cells (Cxcl10, Cxcl9, Ccl12, and Ccl5), BBB integrity (Icam1, Jam1, Mmp3, and Mmp13), and inflammatory response (Gfap, IL6, Tnf, and Gzmb; Figure 1H). Real-time qPCR further validated that two selected DEGs secreted by reactive microglia (TNF-α) and astrocyte (CXCL10)[36] were significantly upregulated in high-titer AAV treated samples (Figures 1I and 1J). Next, significant DEGs were analyzed by Kyoto Encyclopedia of Genes and Genomes (KEGG) and gene otology (GO) for functional classification. KEGG analysis revealed that DEGs were most enriched in immune response pathways, which involved recruitment and functional genes related to immune cells (Figure 1K). The GO category enrichment analysis showed that these DEGs were enriched in biological processes including the immune system process, immune response, regulation of immune effector process, leukocyte activation, cytokine production, and response to cytokine (Figure S1A). Further gene set enrichment analysis (GSEA) revealed that gene sets of T cell activation and differentiation were highly activated in high-titer AAV treated mouse brain (Figures S1B–S1E), suggesting immune cell invasion in the brain parenchyma. CD45 is the leukocyte common antigen and expressed by all hematopoietic cells, except erythrocytes, having a higher level of expression on immune cells. As expected, CD45$^+$ leukocytes were not observed at the site of the low-titer AAV injected mice, while a massive amount of CD45$^+$ leukocytes were detected in brain parenchyma in high-titer AAV treated mice (Figure S1F). Together, these findings indicate that high-titer AAVs lead to transcriptional changes

Figure 1. High-titer AAVs activate a strong anti-viral response in the adult mouse brain

(A) Low-magnification confocal images of GFP (green) at 30 dpi of low-titer (middle) and high-titer AAVs (right) intracranial injection. Scale bar, 200 μm. The left panel is the high-magnification confocal image of GFP co-stained with astrocytic marker S100β (red). Arrowheads indicate GFP-expressing astrocytes. Scale bar, 20 μm. (B) Quantified data of GFP covered area of AAV-infected mouse cortex. (C) Immunostaining of GFAP, Iba1, and CD68 in the AAV injected areas (30 dpi). Scale bar, 20 μm. (D) Quantification of GFAP, Iba1, and CD68 covered area within the injected sites. (E) Experimental schedule. PBS or low- or high-titer AAV9 were injected in the adult mouse cortex and the samples were collected at 10 dpi for further analysis. (F) Bar graph showing DEGs in PBS, 10^8 GC, and 10^{10} GC groups. There are more than 1,000 DEGs between the high-titer group and the PBS or 10^8 GC group. (G) Heatmap showing the top 30 DEGs in the 9 individuals. (H) The DEGs between high- and low-titer AAVs are plotted in the volcano map. Example genes are labeled in black corresponding to blue dots. Note, many DEGs are involved in antiviral, chemokine, BBB, and inflammatory cytokine biological activities. (I and J) qRT-PCR further demonstrated that two of the selected DEGs, TNF-α (I) and Cxcl10 (J), were dramatically upregulated in high-titer AAV treated mice (n = 3 mice per group, $p < 0.01$). (K) The KEGG-enriched bar graph showing the pathways by which high-titer virus elicited an immune response. Statistics were performed using one-way ANOVA analysis with Tukey test (post-hoc).

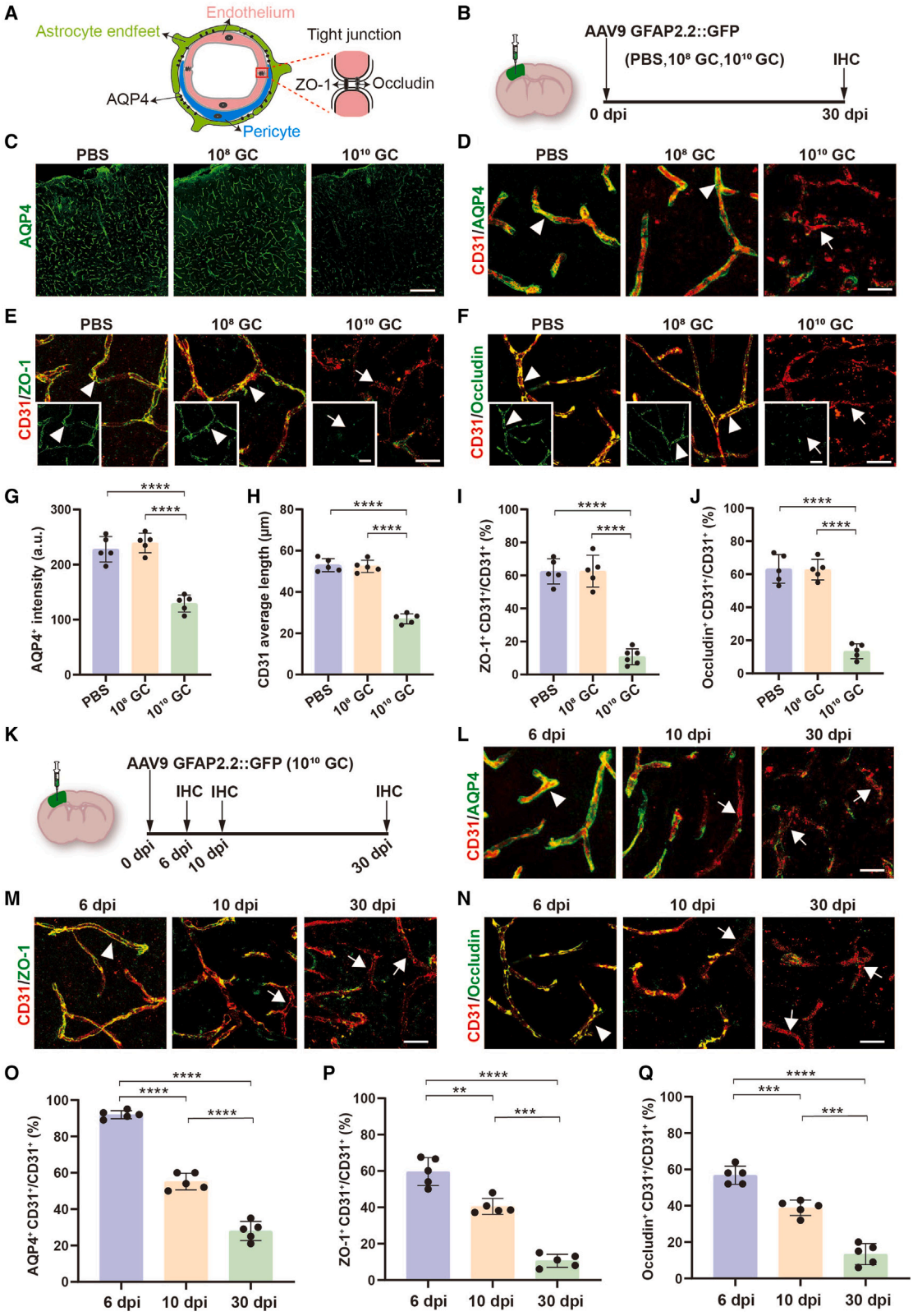

(legend on next page)

of genes involved in immune responses along with leukocyte infiltration.

Overall, we injected AAV9 into the mouse brain at commonly used doses and found that high-titer AAV injection significantly activated astrocytes and microglia. In addition, we also found many DEGs that are involved in BBB integrity and anti-viral immune responses, promoting us to further investigate the potential effects of AAV on BBB and immune responses in the adult mouse brain.

High-titer AAV damages cerebral blood vessels

Normally, leukocyte migration across the BBB is highly restricted and strictly regulated.[22,37] It is thus possible that leukocyte infiltration into brain parenchyma after high-titer AAV injection is due to BBB breakdown. The BBB consists of specialized brain microvascular endothelial cells, which are connected by tight junctions and wrapped by pericytes and astrocytic endfeet (Figure 2A). To investigate the effects of AAV on cerebral blood vessels, we injected different titers of AAV9 into the adult mouse cortex, and samples were collected at 30 dpi for histologic study (Figure 2B). Because dysfunction of astrocytes and pericytes are involved in BBB disruption during CNS inflammation and viral infection, we first performed immunostaining for AQP4, a water channel at astrocytic endfeet,[20] and discovered a significant reduction of AQP4 in high-titer AAV treated mice (Figures 2C and 2G). In PBS or low-titer treated mice, AQP4 expression was detected in the $CD31^+$ endothelial lining of the vasculature, whereas the vascular endothelial cells lost the AQP4 sheath in high-titer AAV treated mice (Figure 2D). Similar to astrocytic endfeet, pericytes ($PDGFR\text{-}\beta^+$) were also tightly attached to the cerebral blood vessels ($CD31^+$) in PBS and low-titer AAV treated mouse brains, but this immunostaining pattern was severely destroyed by the high-titer AAV intracranial injection (Figure S2). Moreover, high-titer AAV injection also resulted in a shortened average length of CD31-labeled blood vessels, indicating that cerebral blood vessels were fragmentized and damaged (Figure 2H). Next, we examined the tight junctions between endothelial cells. Tight junction proteins (ZO-1 and occludin) were present in about 60% of vascular territories in PBS and low-titer treated mouse brains, but were largely reduced in the high-titer AAV treated mice (Figures 2E, 2F, 2I, and 2J). Therefore, high-titer AAV damages the normal structures of cerebral blood vessels.

To elucidate the progress of the BBB disruption by high-titer AAV injection, we selected three time points (Figure 2K). At 6 dpi, we did not find any obvious changes in astrocytic endfeet (AQP4) and tight junctions (ZO-1 and occludin), but a significant reduction of AQP4, ZO-1 and occludin was observed at 10 dpi and these abnormal changes were further exacerbated at 30 dpi (Figures 2L–2N, quantified in Figures 2O–2Q). Together, these data indicate that high-titer AAV induced BBB breakdown starts 6 days after AAV injection.

AAV disrupts the BBB

The integrity of the BBB plays a pivotal role in maintaining the homeostasis of the brain microenvironment. Next, we investigated whether a damaged BBB induced by high-titer AAV injection might lead to the leakage of blood components. Circulating blood is rich in a variety of blood cells and plasma proteins, such as red blood cells, leukocytes, platelets, and immunoglobulins. Normally, these components are difficult to detect in the brain parenchyma due to the restriction of the BBB. Therefore, we first examined IgG, the most abundant immunoglobulin protein in the blood, in the mouse cortex following AAV injection at 30 dpi. We found a more than 4-fold increase in IgG signal in mice injected with high-titer AAVs compared with PBS/low-titer AAVs (Figures 3A and 3B; n = 5 mice). Next, we examined platelet cells ($CD41^+$),[38] a small blood cell with no obvious nucleus ($DAPI^-$), and also found platelets present in the brain parenchyma of high-titer AAV treated mice, but this abnormal phenomenon did not appear in low-titer AAV treated mice (Figures 3C and 3D). Thus, these results suggest that high-titer AAV disrupts the integrity of the BBB and enables components in circulating blood to enter the brain parenchyma.

Increased blood contents in brain parenchyma of high-titer AAV treated mice indicates impairment of the BBB. To further characterize leakage of the damaged cerebral blood vessels, we retro-orbitally injected fluorescent tracers into the mice at 30 days post AAV injection. First, we injected cadaverine and examined its efflux to brain parenchyma after 2 h (Figure 3E). Consistently, astrocytic endfoot marker protein AQP4 was dramatically decreased in high-titer AAV injected brain region, and a large amount of cadaverine was detected in the AQP4 low expressed areas (Figure 3F). Quantified data showed that cadaverine was rarely observed in PBS or low-titer

Figure 2. High-titer AAV destroys BBB biological structures

(A) Diagram of BBB structure including astrocytic endfeet, pericytes, and tight junctions between endothelial cells. (B) Intracranial injection site, the serotype of AAV, and experimental timeline. (C) Representative low-magnification confocal images of focal areas of astrocytic endfeet (AQP4, green) in PBS and AAV injected regions, and robust AQP4 signals were lost in high-titer AAV treated mice. Scale bar, 200 μm. (D–F) High magnification confocal imaging of CD31 (endothelial cell marker, red) co-stained with AQP4 (D) (green), ZO-1 (E) (tight junction marker, green), and occludin (F) (tight junction marker, green) in PBS, 10^8 GC and 10^{10} GC groups. Arrowheads indicate endothelial cells that are wrapped by astrocytic endfeet (D) and sealed by ZO-1 (E) and occludin (F). Arrows indicate the endothelial cells that lost these structures after high-titer AAV injection. Scale bar, 20 μm. (G and H) Quantified data showing the intensity of AQP4 (G) and average length of CD31 (H) in different groups. (I and J) Quantified data showing the ratio of total $ZO\text{-}1^+$ signals to total $CD31^+$ signals (I) and the ratio of total $occludin^+$ signals to total $CD31^+$ signals (J) in different groups. These data reveal that the biological structure of the BBB is disrupted by high-titer AAVs. (K) Study design to examine effects of high-titer AAV injection into the cortex. (L–N) High-magnification confocal imaging of CD31 (endothelial cell marker; red) co-stained with AQP4 (L) (green), ZO-1 (M) (green), and occludin (N) (green) at 6, 10, and 30 dpi. Arrowheads indicate the typical BBB structure that contains astrocytic endfeet and tight junctions at 6 dpi after high-titer AAV injection. Arrow indicates the abnormal BBB that lost these signals starting at 10 dpi after high-titer AAV injection. Scale bars 20 μm. (O–Q) Quantified data showing the ratio of cerebral blood vessels that are surrounded by astrocytic endfeet (O), sealed by ZO-1 (P) and occludin (Q) at different time points after high-titer AAV injection. Values are shown as mean ± SD. n = 5 mice per group. One-way ANOVA analysis with Tukey test. Significance reported as $^{**}p < 0.01$, $^{***}p < 0.001$, $^{****}p < 0.0001$.

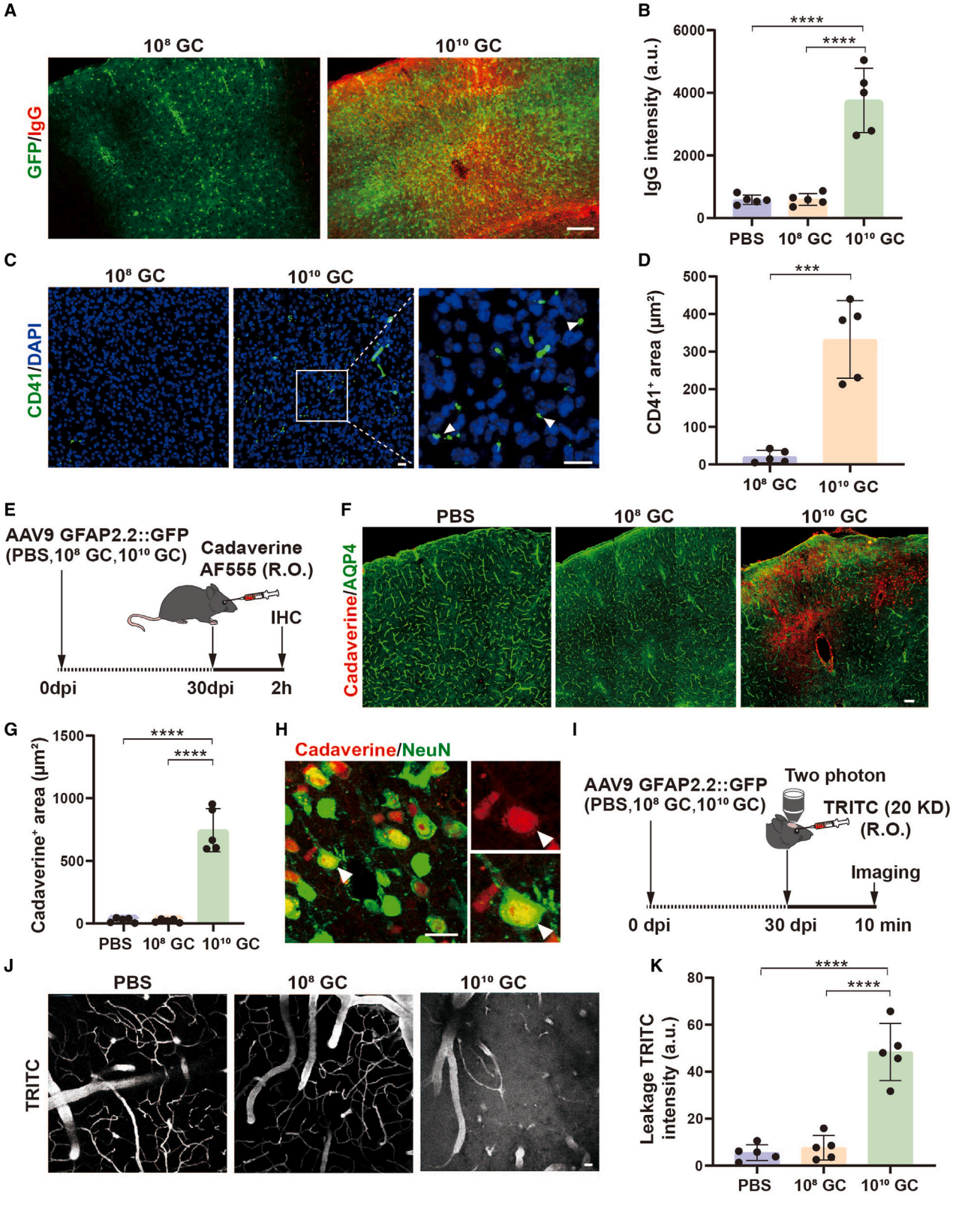

(legend on next page)

AAV injected cortical areas, but was found spreading widely in high-titer AAV injected cortical areas (Figure 3G). Further study found that extravasated cadaverine localized to neurons (Figure 3H). Moreover, we further examined the BBB integrity in living animal brain by using two-photon imaging 10 min after injection of TRIC-conjugated dextran (Figure 3I, 30 dpi). As expected, the fluorescence signal was restrained inside cerebral blood vessels in PBS and low-titer AAV treated mice; however, apparent leakage of dextran was detected outside the blood vessels in high-titer AAV treated mice (Figure 3J, quantified in Figure 3K). Together, these experiments demonstrate that high-titer AAV disrupts the integrity of the BBB and increases the permeability across the BBB.

Lymphocytes infiltrate AAV infected areas

We have shown leukocyte ($CD45^+$) invasion in high-titer AAV treated mouse brain (Figure S1F). To further characterize the infiltrated leukocytes in more detail after AAV injection, we injected three different titers of AAV into the mouse brain and collected the samples for histologic study at 30 dpi. Interestingly, GFP fluorescence was detected in all groups, which indicated that the transgene was expressed after AAV injection. Moreover, we observed robust $CD45^+$ immunostaining signals that were accumulated inside the GFP^+ area in high-titer AAV treated mice (Figures 4A and 4C). By taking high-magnification confocal images, we found a large number of $CD45^+$ cells in the cortex of high-titer (10^{10} GC) AAV injected mice, while very few $CD45^+$ cells were detected in low (10^8 GC) or medium-titer AAV (10^9 GC) treated mice (Figures 4B and 4D). CD45 is a cell surface antigen expressed on most cells of hematopoietic lineage, and resting and activated microglia.[39] To identify the subtypes of these $CD45^+$ cells, we performed co-immunostaining for CD45 and Iba1 and found that more than 90% of $CD45^+$ cells were Iba1 negative (Figures 4E and 4F), suggesting that the majority of $CD45^+$ cells in the brain parenchyma after high-titer AAV injection were infiltrating peripheral leukocytes.

After high-titer AAV injection, it is unclear when leukocytes start to invade the brain parenchyma. To address this topic, we injected high-titer AAV into the mouse cortex and collected brain samples for immunostaining at different times (Figure 4G). At the early time of 6 dpi, we found a few infiltrated $CD45^+$ leukocytes in the brain parenchyma, which was dramatically increased at 10 dpi and then further increased at 20 and 30 dpi (Figures 4H and 4I). Leukocytes, also known as white blood cells, are a group of cells in the immune system, including lymphocytes (T and B cell). Next, we asked what types of leukocytes were involved in these invaded $CD45^+$ cells. To clarify the type of infiltrating leukocytes, we selected different immune cell markers to co-stain with CD45, including CD8 for cytotoxic T lymphocytes (CTLs) and NK cells, CD4 for helper T cells, and CD19 for B cells.[40] Consistently, $CD8^+$ and $CD4^+$ immune cells were detected at 6 dpi, and then sharply increased at 10, 20, and 30 dpi (Figures 4J–4L). Interestingly, the proportion of $CD8^+$ cells remained consistent at different time points (Figure 4M), while the proportion of $CD4^+$ cells gradually increased (Figure 4N). At 30 dpi, we also assessed the B cell population by checking bulk RNA-seq data and CD19 immunostaining, we found that B cell activation and differentiation were increased (GSEA, Figures S3A and S3B), and about 13.6% infiltrating lymphocytes were $CD19^+$ B cells (Figures S3C–S3F). In line with our bulk RNA-seq finding, these results reveal that after high-titer AAV injection, a diversity of immune cells, including $CD8^+$ and $CD4^+$ T cells, infiltrate into brain parenchyma.

Universality of cerebrovascular toxicity induced by high-titer AAV

Different GFAP promoters (2.1 kb, 1.6 kb, and 681 bp) are commonly used to drive transgene expression in astrocytes.[31,41] A previous study found that the cytotoxicity induced by AAVs in the retina might be correlated with the promoter in the AAV genome.[42] Therefore, we asked whether high-titer AAV induced BBB breakdown and leukocyte infiltration might also be associated with promoters in AAV vectors. Then we injected AAVs with two shorter versions of astrocyte specific promoters, 1.6 kb in AAV9 (Figure S4A) and 681 bp in AAV5 (Figure S4E), into the mouse cortex. Similar to that found for the long promoter (2.1 kb) in AAV9, we found a severe AQP4 signal loss and leukocyte infiltration at the site of high-titer AAV injected regions compared with low-titer AAV treated mice (Figure S4). Thus, BBB disruption and leukocyte infiltration induced by high-titer AAV seems to be unrelated to different forms of GFAP promoter.

Given that different brain regions have their own characteristics in structure, cellular composition, and function, we asked whether

Figure 3. High-titer AAV results in BBB leakage

(A) Low-magnification Zeiss fluorescence microscope showing that IgG (red) enters the brain parenchyma in 10^{10} GC groups. GFP (green) indicates the AAV infected brain area. (B) Quantification of IgG immunofluorescence intensity. (C) Typical confocal imaging of CD41 (platelet marker, green) signal in 10^8 GC (left) and 10^{10} GC (right) groups at 20 dpi; infiltrated platelets were observed clearly in high-titer AAV treated mouse brain. Arrowheads indicate some typical platelets that are lacking DAPI. Scale bars 20 μm. (D) Quantification of platelets, showing a significant increase in infiltrated platelets in high-titer AAV treated mouse brain (***$p < 0.001$, two-tailed Student's t test). (E) Assessment of BBB permeability with cadaverine Alexa Fluor 555 dye. Cadaverine was injected through the retro-orbital venous sinus at 30 dpi of AAV/PBS injection, and circulated for 2 h. Then mice were sacrificed for immunohistochemistry. (F) Low-magnification confocal imaging of cadaverine (red) co-stained with AQP4 (green) at 30 days. Extravasated cadaverine was detected in the high-titer AAV injected cortical area, where astrocytic endfeet (AQP4) were also reduced. Scale bar, 20 μm. (G) Quantifications of extravasated cadaverine area. (H) High-magnification confocal imaging of cadaverine (red) co-stained with NeuN (green) at 30 days. Scale bar, 20 μm. (I) Assessment of BBB permeability with two-photon microscopy. Thirty days after AAV injection, TRITC (20 kDa) was injected through the retro-orbital venous sinus, and then imaged immediately for 10 min. (J) Two-photon microscopy of 20 kDa dextran (white) in cortical blood vessels in the PBS, 10^8 GC, and 10^{10} GC groups. Note that TRITC fluorescence signal was detected not only in blood vessels but also in brain parenchyma in high-titer AAV injected mice. Scale bar, 20 μm. (K) Quantifications of leakage TRITC intensity. Values are shown as mean ± SD. n = 5 mice per group. One-way ANOVA analysis with Tukey test was performed in (B, G, and K). Significance is reported as ***$p < 0.001$, ****$p < 0.0001$.

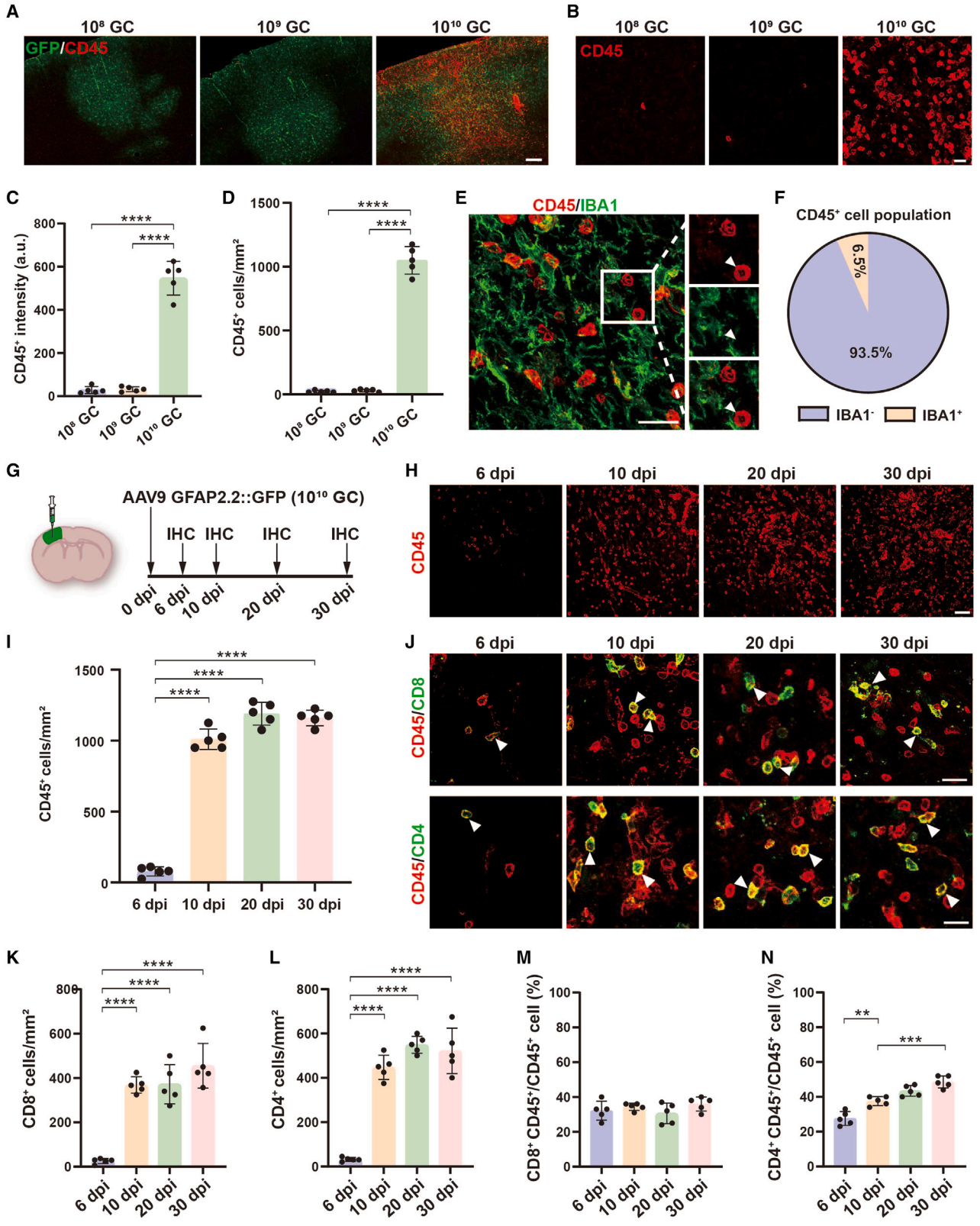

(legend on next page)

exposure to the same high-titer of AAVs in different brain regions would elicit similar changes such as BBB breakdown and leukocyte infiltration. Therefore, we injected AAV9 (10^8 GC and 10^{10} GC) into the mouse striatum and hippocampus, two of the brain regions that were frequently injected with AAVs for studying neuroscience (Figures 5A and 5B). Damaged BBB were also detected clearly both in the striatum and hippocampus in high-titer AAV9 injected areas (Figures 5C, 5D right, and 5E), but not in low-titer AAV9 injected mice (Figures 5D left and 5E). Upon BBB breakdown, we also observed much $CD45^+$ leukocyte infiltration in brain parenchyma of striatum and hippocampus after high-titer AAV intracranial injection (Figures 5F, 5G right, and 5H). Invaded leukocytes were not observed in low-titer AAV9 treated mice (Figures 5G left and 5H). Next, to exclude any potential contribution of AAV serotypes, we injected AAV5 (10^8 GC and 10^{10} GC), another serotype of AAV that is also commonly used in the adult mouse brain, into the cortex (Figure S5A). At 30 dpi, a large amount of GFP was expressed around the AAV5 injected site (Figure S5B). As expected, we also found injured cerebral blood vessels (Figures S5C, S5D right, and S5G) and invaded immune cells (Figures S5E, S5F right, and S5H) in high-titer AAV5 injected mouse cortex, but these side effects were not detected in low-titer AAV5 treated mice (Figures S5D left, and S5F left). Moreover, to examine the effect of injecting volume on the BBB, high-titer AAV9 (10^{13} GC/mL) with different volumes (0.1 and 0.5 μL) were microinjected into the mouse cortex (Figures S6A and S6B). Interestingly, both AQP4 reduction and lymphocyte infiltration were also observed at the core of the injection area (Figures S6C–S6F). Together, these results suggest that high-titer AAV induced cerebrovascular toxicity and leukocyte infiltration are widespread in the adult mouse brain.

Neuronal injury in AAV injected area

The infiltration of lymphocytes in the brain parenchyma after high-titer AAV injection led us to investigate whether these infiltrated immune cells, especially CTLs, can attack the local neurons to induce neurotoxicity. Granzyme B (GZMB), a serine protease normally released by NK cells and cytotoxic T cells, activates apoptosis in target cells.[43,44] Our bulk RNA-seq data have shown that the GZMB gene is significantly upregulated by high-titer AAV injection (Figure 1H). To further confirm GZMB expression, we performed GZMB immunostaining from 10, 20, and 30 dpi of high-titer AAV injected mice (Figure 6A) and found many $GZMB^+$ cells in AAV injected areas at 20 and 30 dpi but not at 10 dpi (Figures 6B and 6E). Next, we found that over 90% of $GZMB^+$ cells were $CD4^+$ (Figures 6D and 6F), but none of the $CD8^+$ cells co-localized with GZMB in AAV injected mouse brain (Figures 6C and 6F). Among these $CD4^+$ lymphocytes, 34% were $GZMB^+$ (Figure 6G). These data suggested that the majority of $GZMB^+$ lymphocytes are $CD4^+$ T cells.

Having acknowledged the cytotoxic role of infiltrated lymphocytes by activating target cell apoptosis,[45,46] we next investigated TUNEL signal, a classic marker of apoptosis, in the mouse brain region of high-titer AAV injection. We found a number of $TUNEL^+$ cells in high-titer AAV injected cortex at 10 dpi but few in PBS-injected areas (Figures 6H and 6I). Further studies revealed abundant TUNEL signaling in neurons at 10 dpi of high-titer AAV injection, suggesting that high-titer AAV triggered neuronal apoptosis (Figure 6J). To elucidate the effect of AAV on neuronal density, we injected PBS and two different titers of AAVs into mouse cortex, then collected brain samples at 10, 20, and 30 dpi for immunostaining (Figure 6K). We found that PBS and low-titer AAV treated mice had no apparent changes in neuronal density at all three time points; however, significant neuronal loss was observed as early as 10 dpi in high-titer AAV treated mice (Figures 6L and 6M). Together, these findings indicate that high-titer AAV induces CTL infiltration and neuronal loss.

AAV cytotoxicity is independent of GFP expression

GFP, an engineered fluorescent protein that is derived from jellyfish Aequorea, has been widely used for cell tracking, but it has also shown cytotoxicity and immunogenicity.[47] Therefore, we asked whether high-titer AAV injection induced BBB disruption and lymphocyte infiltration were the result of GFP overexpression rather than the immunogenicity of AAV. To answer this possibility, we employed the Cre-Flex system, in which GFP expression is driven by the CAG promoter and controlled by Cre recombinase (Figure 7A). Then, we injected high-titer AAV9 into either Cre77.6 transgenic mice (mGfap-Cre, Cre expressed in astrocytes) to induce GFP expression or wild-type mice without GFP expression (Figure 7B). Indeed, we found robust GFP expression in mGfap-Cre transgenic mice but not in wild-type mice (Figure 7C), indicating that Flex-GFP is not expressed in wild-type mice. Interestingly, when we examined the cerebral blood vessels (Figures 7D and 7E), lymphocyte infiltration (Figures 7F and 7G), invaded GZMB-expressing leukocytes (Figures 7H and 7I), and neuronal toxicity (Figures 7J and 7K), we found significant abnormal changes in wild-type mice as well, and these changes were comparable with mGfap-Cre transgenic mice. In addition, we also injected high

Figure 4. High-titer AAV induces immune cell infiltration

(A) Low-magnification Zeiss fluorescence microscope imaging of GFP (green) co-stained with CD45 (red) at 30 dpi of AAV injection. Note that many infiltrated leukocytes were present in high-titer AAV treated mice. Scale bar, 200 μm. (B) Confocal images of CD45 immunostaining in 10^8 GC, 10^9 GC, and 10^{10} GC groups. Scale bar, 20 μm. (C and D) Quantifications of CD45 fluorescence intensity (C) and $CD45^+$ cell density (D) in 10^8 GC, 10^9 GC, and 10^{10} GC groups. (E) High-magnification confocal image of CD45 (red) co-stained with IBA1 (green) at 30 days after high-titer AAV injection. Arrowhead indicates a typical infiltrated lymphocyte that is lacking Iba1. Scale bar, 20 μm. (F) Pie chart showing that 93.5% of CD45 positive cells were Iba1 negative. (G) Experimental design. (H) Low-magnification confocal images of CD45 signal at different time points. Scale bar, 50 μm. (I) Quantifications of $CD45^+$ cell density at different time points. (J) High-magnification confocal images of CD45 (red) co-stained with CD8 (green, upper row), and CD45 (red) co-stained with CD4 (green, bottom row) at different time points. Arrowheads indicate some infiltrated lymphocytes co-labeled with CD8 (top) and CD4 (bottom) T cell antigens. Scale bars, 20 μm. (K and L) Quantifications of $CD8^+$ and $CD4^+$ cell density at different time points. (M and N) Quantifications of the percentage of CD8 and CD4 positive cells. Values are shown as mean ± SD. n = 5 mice per group. One-way ANOVA analysis with Tukey test. Significance reported as $^{**}p < 0.01$, $^{***}p < 0.001$, $^{****}p < 0.0001$.

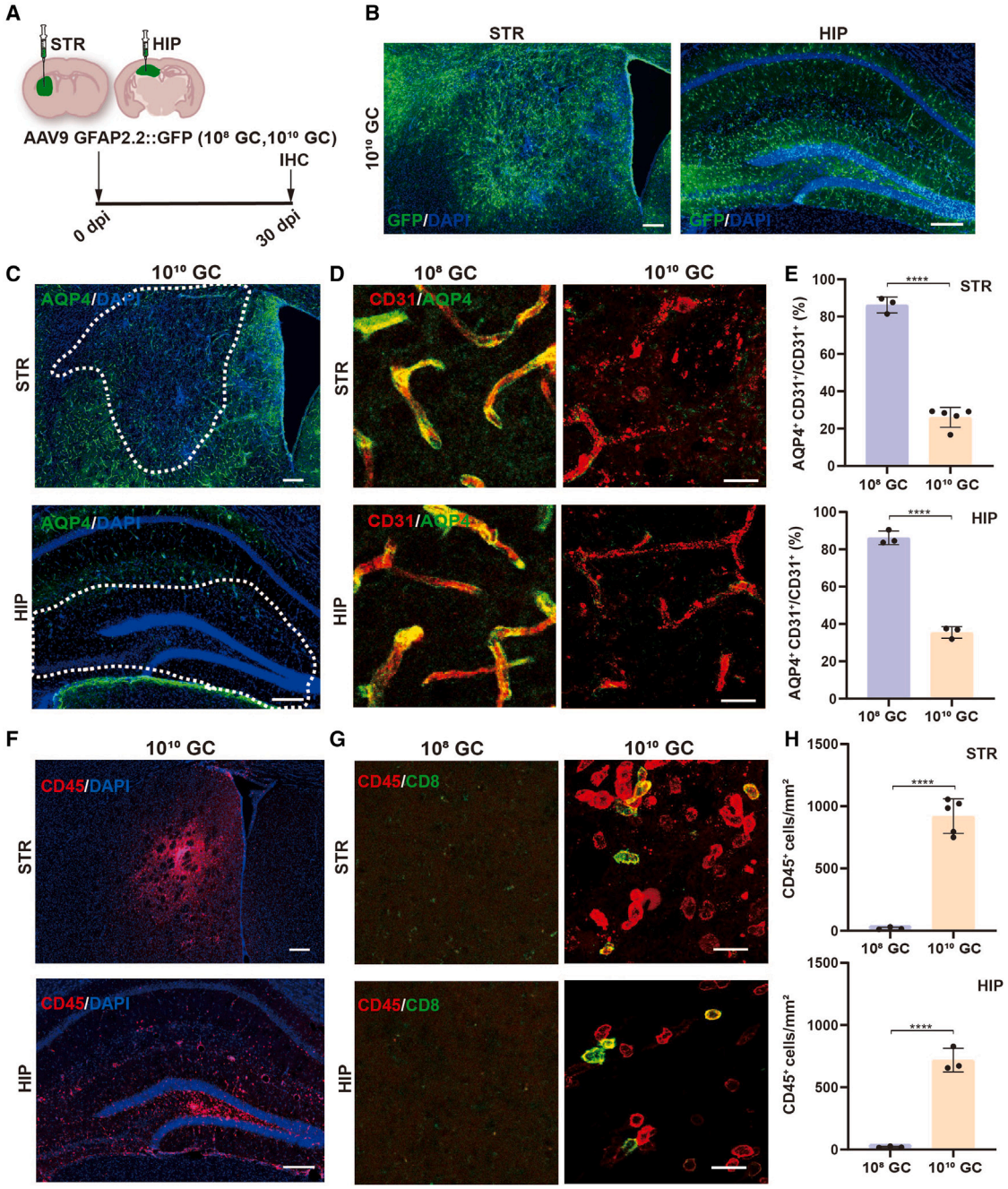

Figure 5. High-titer AAV injection results in BBB disruption and leukocyte invasion in striatum and hippocampus

(A) Experimental timeline. (B) GFP expression in striatum and hippocampus at 30 days post AAV injection. Scale bars, 200 μm. (C) AQP4 immunofluorescence (green) in striatum (top) and hippocampus (bottom) of high-titer AAV9 injected mice. White dashed boxes indicate the high-titer AAV injected areas where AQP4 was drastically reduced. Scale bars, 200 μm. (D) Immunofluorescence of CD31 (endothelial cells, red) and AQP4 (astrocytic endfeet, green) in striatum and hippocampus after low-titer (left) and high-titer AAV9 (right) injection. These confocal images revealed that the perivascular astrocytic endfeet were lost within brain parenchyma after high-titer AAV9 injection. Scale bars, 20 μm. (E) Quantification data show that perivascular astrocytic endfeet are significantly reduced in high-titer AAV injected mice. (F) Low-magnification confocal images showing CD45-positive leukocyte infiltration into the striatum (top) and hippocampus (bottom) after high-titer AAV9 injection. Scale bars, 200 μm. (G) High-magnification images showing that some of the infiltrated $CD45^+$ leukocytes (red) are $CD8^+$ T cells (green) were detected only in brain regions injected with high-titer AAV9 but not in low-titer AAV9 injected brain regions. Scale bars, 20 μm. (H) Statistical analysis shows that high-titer AAV injection results in significant leukocyte infiltration both in striatum and hippocampus. Data are shown as mean ± SD. n = 3 or 5 mice per group. Two-tailed Student's t test. Significance reported as ****$p < 0.0001$.

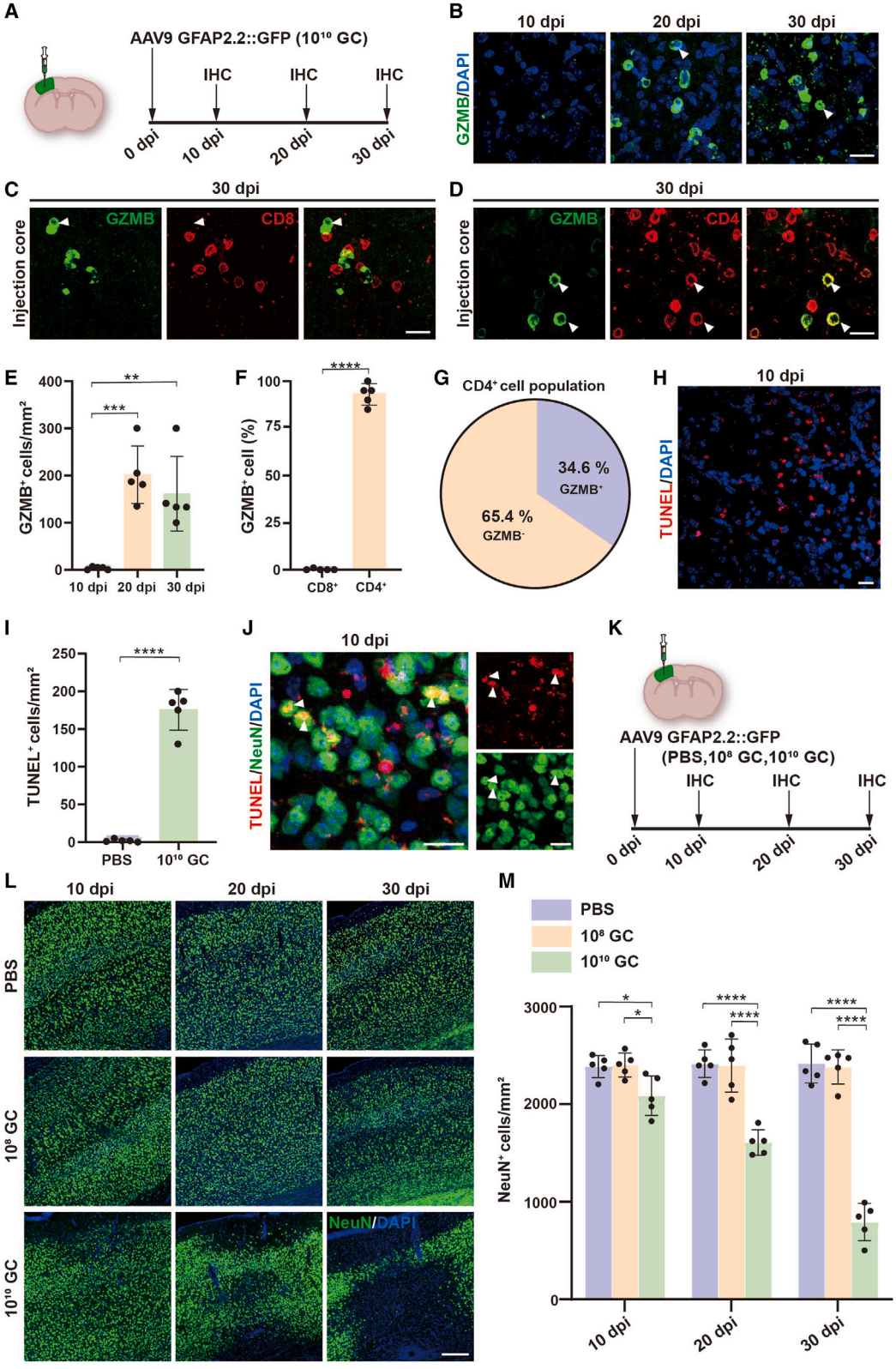

(legend on next page)

titers of AAV5-Flex-GFP (10^8 GC and 10^{10} GC) into wild-type mice (no GFP expression) to further test the influence of different serotypes of AAVs, and found similar cerebral vascular damage and lymphocyte infiltration in high-titer AAV5 treated mice but not in low-titer AAV5 treated mice (Figure S7). Therefore, these results demonstrate that the high-titer AAV induced cytotoxicity and lymphocyte infiltration are independent of GFP expression.

Although the absence of GFP can still cause cerebrovascular toxicity after injection of AAV-CAG::Flex-GFP, the DNA of AAV still enters the host cells. Several studies have shown that DNA immunosensors can detect the AAV genome and elicit innate immunity and T cell responses.[48–50] We then wondered whether the toxicity was due to the AAV capsids themselves or to the DNA backbone packaged in the capsids. Therefore, the empty AAV9 viral capsids (1 μL) were injected into the adult mouse cortex at two different titers (10^{11} and 10^{13} capsids/mL), and the samples were collected at 30 dpi for histologic study (Figure S8A). Injection of empty AAV9 viral capsid alone did not result in BBB breakdown (Figures S8B and S8C) and lymphocyte invasion (Figure S8D). These results suggest that viral DNA is required for high-titer AAV induced BBB disruption and lymphocyte infiltration, but independent of the transgene expression.

Reducing infiltrated lymphocytes decreases neurotoxicity

Our data implicate an association between lymphocyte infiltration and neuronal loss in high-titer AAV treated mouse brain, but it is unclear whether invaded immune cells are directly involved in loss of neurons. To this end, we treated mice with anti-CD8 or anti-CD4 depleting antibodies beginning at 5 dpi after AAV injection (Figure 8A), a time selected to precede the immune cell infiltration (Figures 4H and 4I). Rat IgG was injected as control.[51–53] These treatments resulted in a significant reduction of $CD8^+$ or $CD4^+$ T cell infiltration in brains 30 days after high-titer AAV injection (Figures 8B–8E). Interestingly, high-titer AAV induced neuronal damage was significantly reduced by inhibition of either infiltrated $CD8^+$ or $CD4^+$ T cells (Figures 8F and 8G). These results suggest that high-titer AAV induced neuronal loss is associated with the infiltrated $CD8^+$ and $CD4^+$ T cells.

GZMB is a caspase like serine protease released by cytotoxic lymphocytes that were enriched in $CD4^+$ T cells in our study (Figure 6D). Therefore, we asked whether blocking GZMB function protects neurons from apoptosis induced by high-titer of AAVs. To test this hypothesis, GZMB functions were inhibited starting at 10 days after high-titer AAV injection by using an anti-GZMB neutralizing monoclonal antibody (intracisternal injection, Figure 8H). Compared with the IgG treated mice, blockade of GZMB function partially attenuated neuronal loss following high-titer AAV injection (Figures 8I and 8J), indicating that inhibiting GZMB function through injection of anti-GZMB neutralizing antibody also can partially alleviate high-titer AAV induced neuronal injury. Taken together, our study reveals that high-titer AAVs disrupt the integrity of the BBB and induce lymphocyte infiltration and neuronal damage in the adult mouse brain (Figure 8K). We also show that suppression of lymphocyte infiltration or blocking GZMB function are potential approaches for alleviating high-titer AAV induced neurotoxicity.

DISCUSSION

Intracranial microinjection of AAVs is considered to be a safe and efficient approach for driving transgene expression in the CNS. However, we show that high-titer AAV injection upregulates many genes involved in disrupting the BBB and activating adaptive immune responses. Further histologic studies revealed that the integrity of the BBB was significantly damaged by the high-titer AAVs. This led to leakage of cerebral blood vessels and lymphocyte infiltration. Lymphocyte invasion, especially CTLs, results in severe neurotoxicity at the site of high-titer AAV injection. By using T immune cell depleting or GZMB neutralizing antibody, high-titer AAV induced neuronal loss was significantly reduced. This is the first study showing the disruption of the BBB and lymphocyte infiltration following high-titer AAV intracranial microinjection in the adult mouse brain.

In this study, we observed disruption of the BBB accompanied by lymphocytic infiltration following AAV intracranial injection, which has never been reported in previous studies. An immediate concern is that infiltrated immune cells reach the injected site through the needle track, because CNS borders including meninges harbor a diverse repertoire of adaptive immune population.[54–57] But this possibility can be easily excluded due to the absence of infiltrated immune cells in PBS, low-titer AAV, and empty AAV capsid injected mice. Moreover, extensive transcriptome abnormalities with prominent signatures of immune responses, such as genes involved in immune cell recruitment, were remarkably upregulated compared with low-titer AAV treated mice. Therefore, these results suggest that immune cells present in the brain parenchyma are induced by high-titer AAV

Figure 6. Infiltrated immune cells cause neurotoxicity

(A) Scheme of immunostaining studies after high-titer AAV injection for examining GZMB-expressing infiltrated immune cells. (B) Confocal images of GZMB (green) at different time points. Arrowheads showing some typical GZMB-expressing cells. Scale bar, 20 μm. (C and D) Confocal images showing GZMB (green) co-stained with CD4 (D, red) but not CD8 (C, red) at 30 dpi. Arrowheads indicate some typical GZMB-expressing cells that are co-expressing CD4 but not CD8. Scale bar, 20 μm. (E) Quantification showing the density of $GZMB^+$ cells at different time points. (F) Summarized data illustrating almost all of the $GZMB^+$ cells belong to $CD4^+$ T cells. (G) Pie chart showing 34.6% of $CD4^+$ T cells containing GZMB in the total $CD4^+$ T cell population. (H) High-titer AAV induced cellular apoptosis was detected by TUNEL staining (red). Scale bar, 20 μm. (I) Quantification data of $TUNEL^+$ cells in PBS and high-titer AAV treated mice. (J) Representative images of TUNEL (red) co-stained with NeuN (green, indicated by arrowheads) in high-titer AAV injected cortex. Scale bars, 20 μm. (K) Experimental design for investigating neurotoxicity at different time points after high-titer AAV injection. (L) Representative images of NeuN (green) in PBS, 10^8 GC, and 10^{10} GC groups at different time points. Scale bar, 200 μm. (M) Quantifications of neuronal density near the injected areas. Note that the neuron density was significantly decreased starting at 10 dpi, then furtherly reduced at 20 and 30 dpi. Data are shown as mean ± SD. n = 5 mice per group. Two-tailed Student's t test was performed in (F and I). One-way ANOVA analysis with Tukey test was performed in (E and M). Significance reported as $^*p < 0.05$, $^{**}p < 0.01$, $^{***}p < 0.001$, $^{****}p < 0.0001$.

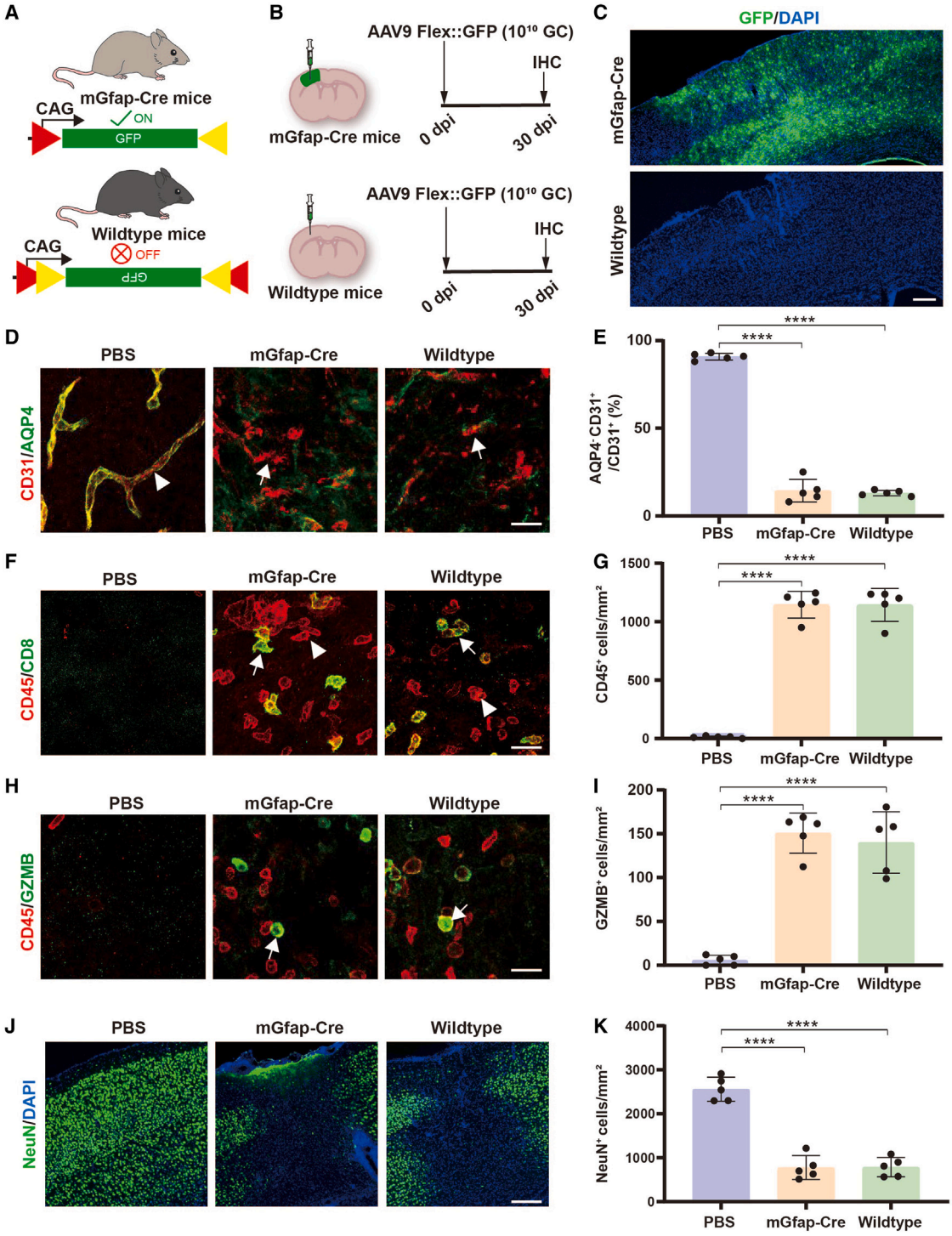

Figure 7. AAV-induced BBB breakdown and neuronal toxicity is independent of GFP expression

(A) Work model of the Cre-Flex system in which the expression of GFP is controlled by the Cre recombinase. (B) Experimental design. (C) Low-magnification Zeiss fluorescence microscope images of GFP (green) signal. Note that GFP was nicely expressed in mGfap-Cre transgenic mouse brain, while no GFP was detected in wild-type mice. Scale bar, 200 μm. (D) Confocal images of CD31 (red) co-stained with AQP4 (green) at 30 dpi in PBS treated mice (left), high-titer AAV treated mGfap-Cre transgenic (middle) and wild-type mice (right). Arrowheads show a fragment of blood vessel wall formed by endothelial cells well wrapped by astrocytic endfeet. Arrows indicate the blood vessel wall lost astrocytic endfeet wrap. Scale bar, 20 μm. (E) Quantified data showing that the AQP4 wrapped cerebral blood vessels were significantly reduced both in mGfap-Cre

(legend continued on next page)

injection, rather than CNS border immune cells migrating along the needle tract to the injection site. The next concern is that high-titer AAV induced BBB disruption and lymphocyte infiltration are closely related to the viral vectors we selected in this study, such as the promoter, exogenous transgene expression (GFP), and serotype.[42,47] This has been carefully considered but found to be incompatible with our observations. First, four different promoters were used in our study, including three astrocyte specific promoters and one non-specific promoter (CAG), and all AAV vectors showed BBB breakdown and immune cell invasion under high-titer conditions. Second, we employed the Flex-GFP vector in our study to exclude the impact of long-term GFP expression on the BBB. Although GFP was not expressed in the brains of wild-type mice following high-titer AAV injections (Figure 6C, bottom), we still noticed BBB breakdown and lymphocyte infiltration. Third, we employed AAV5, another widely used serotype in neuroscience research, to further validate our findings. Consistent with the findings of AAV9, high-titer AAV5 injection also can induce BBB breakdown and lymphocyte infiltration. Altogether, these findings suggest that high-titer AAV is the direct inducement for BBB disruption and lymphocyte infiltration.

The brain is often described as immune-privileged due in part to the presence of a BBB that limits the entry of immune cells. Therefore, the adaptive immune response induced by AAV in the brain parenchyma is usually disregarded.[58] Nevertheless, our study clearly shows that high-titer AAV intracranial injection results in disruption of the BBB and immune cell infiltration, and then leads to neuronal toxicity. Accordingly, a previous study has shown that high-titer AAV injection resulted in a prominent decrease of astrocytic glutamine synthetase,[29] suggesting that the normal function of astrocytes is disturbed by the high-titer of AAV. Given that astrocytic endfeet are the critical cellular structure for maintaining the integrity of the BBB, high-titer AAV induced astrocyte dysfunction may also disrupt BBB integrity. To provide the molecular and histologic substrate, we found that another astrocytic protein, AQP4, was also remarkably reduced at high-titer AAV injection sites. Normally, water channel AQP4 is primarily expressed at perivascular astrocytic endfoot processes around the BBB,[18] while astrocytic AQP4 reduction indicates BBB dysfunction. Thus, our study extends previous findings from astrocytes to BBB, and provides the first piece of evidence for high-titer AAV injection induced BBB disruption, an unwanted adverse reaction that has never been reported by previous studies.

In general, AAV vectors safely transduce CNS and retina, but the evidence is accumulating that AAV-based gene delivery can cause unexpected adverse effects in these nervous systems,[4,6,42,48] but the mechanisms are not yet fully understood. For example, a recent study found that high-dose AAV injection in adult mouse hippocampus resulted in ablation of neurogenesis;[59] however, how high-dose AAV impairs hippocampal neurogenesis has not been elucidated. Interestingly, activated T cell released GZMB has been found to inhibit hippocampal neurogenesis.[60] Given the findings of $GZMB^+$ T cells present at the sites of high-titer AAV injection in our study, it is expected that AAV induced neurogenesis ablation is caused by the infiltrated $GZMB^+$ T cells. Moreover, this working model may also help to explain other AAV induced unexpected reactions in CNS such as neuronal toxicity.[61] Since AAVs have been widely used in both basic neuroscience research and gene therapy for neurological disorders, including neuronal circuits,[62,63] *in vivo* glia-to-neuron conversion,[64–66] and gene therapy,[1,3,14,67,68] as well as producing animal models of neurodegenerative disease.[69–71] Meanwhile, intracranial injection of high-titer AAV ($\geq 10^{13}$ GC/mL) is frequently used in neuroscience studies. Therefore, we call on researchers to consider the possible impact of viral titer on experimental results when using AAV as a gene delivery vector to avoid misinterpretation of experimental results.

The recent advances in AAV modification technology have promoted the emergence of many new engineered AAV serotypes for targeting the CNS.[2,72] One of the major improvements involves increasing the target specificity of AAVs and reducing the possibility of non-target cells.[73,74] Therefore, the first limitation of our study is the fact that the new generation of modified AAVs were not investigated. In addition, BBB crossing AAV serotypes were developed by scientists, and the broad transduction in the CNS was achieved after systemic injection.[75,76] However, whether systemic injection of a large amount of BBB crossing AAVs would also result in disruption of the BBB and lymphocyte invasion is not investigated, this is the second limitation. Moreover, our bulk RNA-seq data revealed many upregulated genes involved in BBB breakdown and lymphocyte infiltration, but we have not yet elucidated what cell type initiates this process, this is the third limitation in this study. In addition, several studies have demonstrated an important role of AAV genomes in triggering host immune response, including promoters, inverted terminal repeat (ITR) sequences, and transgenes[48–50]; however, we did not touch on such details. Therefore, further investigations will be needed to decipher the relative contribution of AAV genomes and capsids in the context of BBB disruption and lymphocyte infiltration. In addition, we demonstrate that administration of T cell depleting antibodies or GZMB neutralizing antibodies can significantly attenuate neuronal

transgenic and wild-type mice after high-titer AAV injection. (F) Confocal images of CD45 (red) co-stained with CD8 (green, indicated by arrows) at 30 dpi in different groups. Arrowheads represent the CD8 negative leukocytes. Scale bar, 20 μm. (G) Quantified data showing that the $CD45^+$ cell density was remarkably increased both in mGfap-Cre transgenic mice and wild-type mice after high-titer AAV injection. (H) Confocal images of CD45 (red) co-stained with GZMB (green, indicated by arrows) at 30 dpi in different groups. Scale bar, 20 μm. (I) Quantified data showing that the $GZMB^+$ cell density was significantly increased both in mGfap-Cre transgenic mice and wild-type mice after high-titer AAV injection. (J) Low-magnification images of NeuN (green) signal. Note that the massive NeuN loss was observed both in mGfap-Cre transgenic mice and wild-type mice after high-titer AAV injection. Scale bar, 200 μm. (K) Quantified data illustrating that the remarkable neuronal loss was presented in both mGfap-Cre transgenic mice and wild-type mice after high-titer AAV injection. Values are shown as mean ± SD. n = 5 mice per group. One-way ANOVA analysis with Tukey test. Significance reported as ****$p < 0.0001$.

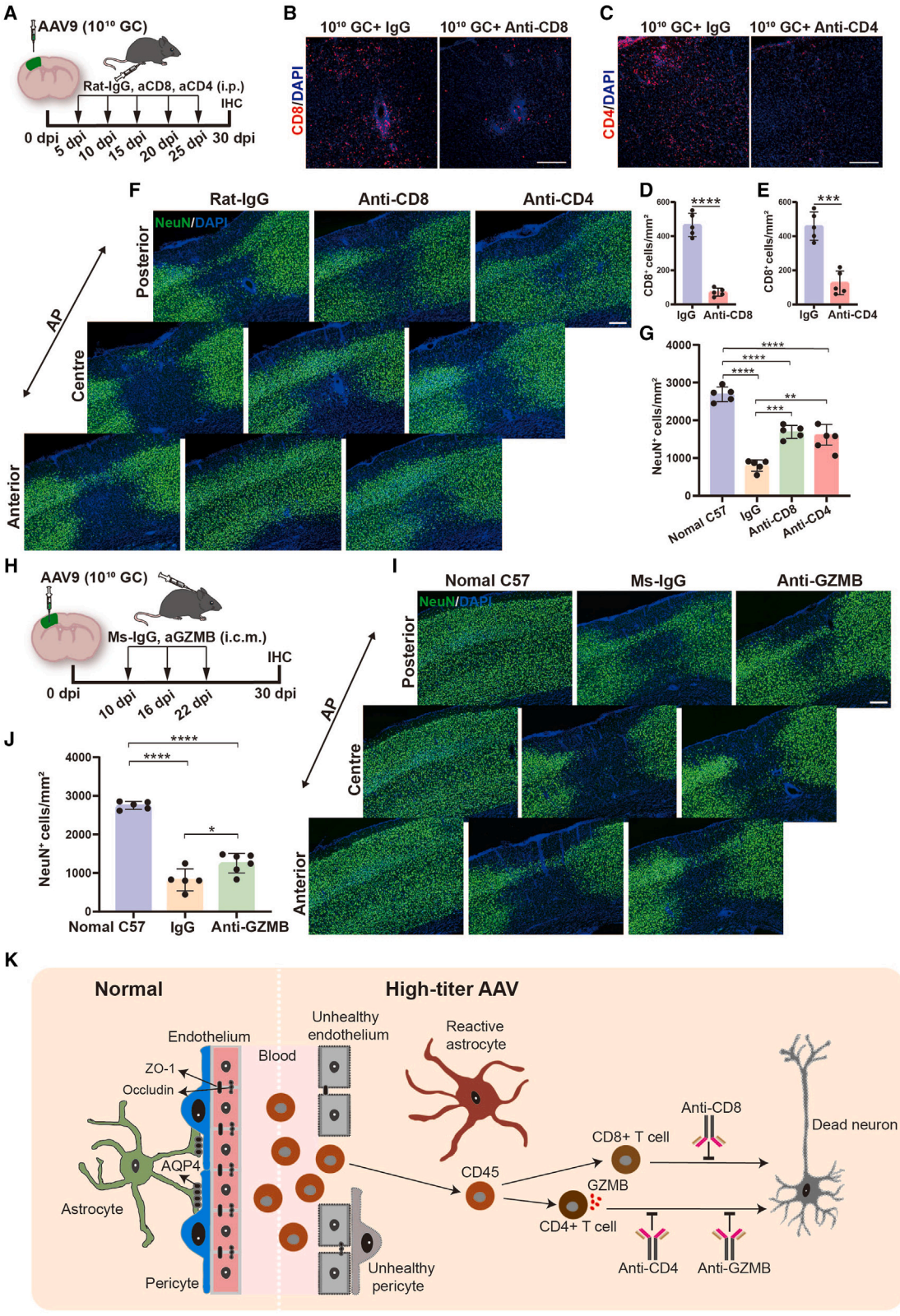

(legend on next page)

toxicity induced by intracranial injection of high-titer AAV; however, we have not systematically investigated the optimal route, dose and frequency of administration, which is another disadvantage of this study. Investigation of the optimal route, dose, and frequency of administration is an important guide for possible future clinical use and deserves further study.

In conclusion, this study reveals that high-titer AAV intracranial injection results in disruption of the BBB and lymphocyte infiltration in the adult mouse brain, followed by neuronal loss at the injection sites, which has never been reported by previous studies. The high-titer AAVs induced unexpected adverse reactions in the adult mouse, suggesting that future work using AAVs as an experimental tool in the adult mouse brain, and as gene therapy for CNS disorders, should be carefully evaluated. Meanwhile, to achieve both safe and effective expression of transgene, we do not need to inject high-titer AAVs ($\geq 10^{13}$ GC/mL) into the mouse brain.

MATERIALS AND METHODS

Animals

Experiments were conducted on adult (age 2–3 months) wild-type C57BL/6J mice (Guangdong Yaokang Biotechnology, China) and 2- to 3-month-old GFAP::Cre transgenic mice (B6.Cg-Tg [Gfap-cre] 77.6Mvs/2J, Cre77.6, Jackson Laboratory). Both male and female mice were used in this study and all mice were subjected to a standard 12 h light and dark cycle with sufficient water and food. Experimental protocols were approved by the Laboratory Animal Ethics Committee of Jinan University, China (approval no. IACUC-20210406-03 and 20220406-07).

AAV vector production and titration

SsAAV vectors were used in this study, and all vector genomes were flanked by AAV2/9 (AAV9) or AAV2/5 (AAV5) ITRs. AAV vectors, GFAP-GFP and CAG-Flex-GFP, were constructed by PackGene Biotech. The versions of the GFAP promoter used in this study included GFAP2.2 (2.2-kb gfa2 promoter), GFAP1.6 (1.6-kb GFAP promoter), and GFAP681 (681-bp gfaABC1D promoter). Recombinant AAV9 and AAV5 were produced by PackGene Biotech. The steps include: first, a large number of ultrapure plasmids were extracted and co-transfected with HEK293 cells. AAV was then concentrated and purified by ultra-high-speed gradient centrifugation. Finally, the virus titer was tested by FWD ITR and REV ITR primer specific detection of AAV vector ITR sequence by SYBR green qPCR and the purity of AAV was determined by SDS-PAGE electrophoresis. The empty AAV9 viral capsids were prepared in the same way, except that the genome plasmid of the vector (*cis*-plasmid) was excluded in the transfection step (PackGene Biotech). The titer of the empty AAV9 viral capsids was determined using an AAV9 Titration ELISA kit (PRAAV9, Progen). Details of the AAVs used in this study are shown in Table S1, including promoter length and original titer. Endotoxin test was performed by gel assay with a test result of less than 10 EU/mL. The purity of capsid protein was determined by SDS-PAGE, and there was no obvious impurity. PBS containing 0.001% F-68 was used for AAV titer adjustment. The AAV9 and AAV5 GC per injection ranged from 10^8 GC to 10^{10} GC. All AAVs were stored in a −80°C freezer and used within 12 months after production.

Stereotaxic viral injection

Brain surgeries were conducted on 2 to 3 month old mice for AAV injection. The mice were anesthetized by intraperitoneal injection of 20 mL/kg 1.25% Avertin (Sigma, T48402). After shaving the hair and washing the scalp with iodine tincture and ethanol, the mice were placed into a stereotaxic setup. Artificial eye ointment was applied to cover the eyes for protection purposes. A midline scalp incision of the mouse brain was made and a drill hole (0.5 mm) on the skull was created for virus injection into the cortex (AP +0.6 mm, ML –2 mm, DV –0.7 mm), striatum (AP +0.6 mm, ML +1.5 mm, DV –3.0 mm), and hippocampus (AP –2.0 mm, ML –1.5 mm, DV –1.5 mm). Using a WPI pump and glass microelectrode, 0.1–1 μL of AAV was injected into the brain at a speed of 100 nL/min. After viral injection, the glass microelectrode was left in the parenchyma for about 10 min and then slowly withdrawn.

Immunofluorescence and analysis

For brain slice staining, the mice were anesthetized with 1.25% Avertin and then sequentially perfused, first with saline solution or ice-cold artificial cerebrospinal fluid to wash the blood off and then with 4% paraformaldehyde (PFA) to fix the brain. Then the brains were quickly removed and post fixed in 4% PFA overnight at 4°C in darkness. After fixation, the samples were cut into 40 μm sections using a vibratome (Leica, VTS1200). Brain slices were washed three times in the phosphate buffer solution for 10 min each and then blocked in the buffer solution (5% donkey serum + 0.5% Triton

Figure 8. Antibody intervention attenuates high-titer AAV induced neurotoxicity

(A) Scheme of antibody intervention. Intraperitoneal administration of CD8 and CD4 depleting antibodies were performed every 5 days after virus injection, the Rat IgG was set as control, then histological studies were performed at 30 dpi. (B and C) Confocal imaging of CD8 signal in IgG and anti-CD8 groups (B), and CD4 signal in IgG and anti-CD4 groups (C). Scale bar, 200 μm. (D and E) Quantifications of $CD8^+$ cell density in IgG and anti-CD8 groups (D), and $CD4^+$ cell density in IgG and anti-CD4 groups (E). (F) Representative microscope images of NeuN (green) signal for control (left), anti-CD8 (middle), and anti-CD4 (right) treated mice. Scale bar, 200 μm. (G) Quantifications of neuron density. Note that the neuronal density was significantly recovered after depleting either $CD8^+$ or $CD4^+$ infiltrated T cells. (H) Experimental design. GZMB and isotype control (Ms IgG) antibodies were injected through the cisterna magna on days 10, 16, and 22 after virus injection, then mice were sacrificed at 30 dpi for histological study. (I) Example images of normal mice (left) and mice that were treated with Ms-IgG (middle) and GZMB neutralizing antibody (right). Scale bar, 200 μm. (J) Quantifications of neuron density in different groups. Statistical analysis indicated that antagonizing GZMB by administering neutralizing antibody also can alleviate high-titer AAV induced neurotoxicity. (K) A schematic illustrating that high-titer AAV disrupts the integrity of the BBB, induces immune cell invasion, and then results in neurotoxicity in the adult mouse brain. Data are shown as mean ± SD. n = 5 mice per group. Two-tailed Student's t test was performed in (D and E). One-way ANOVA analysis with Tukey test was performed in (G and J). Significance reported as $^*p < 0.05$, $^{**}p < 0.01$, $^{***}p < 0.001$, $^{****}p < 0.0001$.

X-100) for 1.5 h at room temperature. Primary antibodies were diluted in the blocking buffer and incubated at 4°C for 24 h (Table S2: primary antibody information). The brain slices were washed three times and then incubated with DAPI and the secondary antibodies conjugated to Alexa Fluor 488, Alexa Fluor 555, or Alexa Fluor 647 (1:1,000) for 1.5 h at room temperature, followed by extensive washing with PBS. The samples were finally mounted on the glass and sealed with nail polish.

IgG immunofluorescence: the animals were treated in the same way as above. The brain slices were washed three times with PBS for 10 min each time, then stained with a secondary antibody (donkey anti-mouse IgG conjugated with Alexa Fluor 555) for 2 h. Brain slices were washed three times with PBS for 10 min each and finally imaged under a Zeiss fluorescence microscope.

The images were acquired using a Zeiss confocal microscope (LSM880, Zeiss, Germany). For mice in the PBS treatment group, mouse brain slices were selected according to the injection coordinates, mouse brain atlas, and needle tract, ensuring that the selected brain slices were close to the injection site (within 300 μm). For quantification, four viral-infected regions in the cortex were randomly taken for confocal imaging (40× lens). The images were analyzed using Zeiss software ZEN and ImageJ software.

BBB permeability assays

Uptake of cadaverine AF555 test

BBB permeability was detected by using 1,000 Da Alexa Fluor 555-cadavirine (A30677, Thermo Fischer Scientific, 50 μL, 1 mg/mL) as a tracer assay. For cadaverine assays, the adult mice were anesthetized with 1.25% Avertin and then the cadaverine was injected into the retro-orbital venous sinus. Cadaverine was allowed to circulate for 2 h in adult mice, then the mice were perfused intracardially with saline solution and 4% PFA. Brain slices were stained in the same way as before. BBB permeability was measured through quantifying the areas of the cadaverine leakage in the virus infected areas.

In vivo *two-photon live imaging analysis*

Thirty days after virus injection, we conducted cranial windows, which were prepared on a vertical laminar flow clean table (SW-CJ-1FD, AIRTECH System). The mice were anesthetized by intraperitoneal injection of 1.25% Avertin. After shaving the hair and washing the scalp with iodine tincture and ethanol, we used a stainless steel head to secure the adapter to fix the head with cyanoacrylate glue. A 2 to 3 mm diameter hole was drilled into the skull surface with a high-speed microdrill (Microdrill 78001, RWD Life Science) and then covered with a cap sleeve (Warner, CS-3R). The skull was then bonded to the cover using Vetbond Tissue Adhesive (3M, 1469SB). Finally, dental acrylic resin (Changshu Shangchi Dental Materials) was used to fix the optical window on the skull. Before imaging, we injected dextran (20,000 Da, Invitrogen, 0.1 mL of 20 mg/mL) through the retro-orbital sinus. *In vivo* time lapse images were acquired every 10 min for a total of 30 min. All images were subjected to threshold processing and the extravascular fluorescent intensity was measured using ImageJ.

A two-photon microscope (Zeiss LM780, Germany) equipped with a Ti:Sapphire laser source (120 fs width pulses, 90 MHz repetition rate, Coherent) was used in our experiments. The mouse was held by an *in vivo* imaging platform (Beijing Xing Lin Biotechnology) during the long repetitive imaging process. The excitation wavelength was set to 1,040 nm. Imaging was achieved using a 20× water-immersion objective (N.A. 1.0, Carl Zeiss, Germany). The image size was 425.10 × 425.10 μm. The image depth was about 60–150 μm from the dura (layer II–IV of the cortex).

qRT-PCR

At 10 days after virus injection, we perfused the mice with ice-cold artificial cerebrospinal fluid. Then the cortical tissue of the virus injection area (0.5 × 0.5 mm) was rapidly harvested and put into 1.5 mL EP tubes in bead-beating tubes containing 1 mm zirconia/silica beads (BioSpec). Tissue was homogenized for 30 s using a mini-bead beater (BioSpec). RNA was extracted according to the manufacturer's instructions (AllPrep, cat. no. 80004). A high capacity reverse transcription kit (transcriptor first-strand cDNA synthesis kit) was used for cDNA synthesis. qRT-PCR was performed with SYBR green fluorescent PCR kit (cat. no. 208054). Reactions were run on a CFX96 Real-Time System (Bio-Rad Laboratories). Relative expression was calculated as $2(-\Delta\Delta CT)$. Primers include:

TNF-α: forward: CTGGATGTCAATCAACAATGGGA

reverse: ACTAGGGTGTGAGTGTTTTCTGT

Cxcl10: forward: ATCATCCCTGCGAGCCTATCCT

reverse: GACCTTTTTTGGCTAAACGCTTTC)

Bulk RNA-seq and analysis

Ten days after virus injection, mice were perfused with ice-cold artificial cerebrospinal fluid. Then the virus infected brain regions were harvested for bulk mRNA-seq and analysis. RNA extraction was done by Gene De novo Biotechnology (Guangzhou, China) (https://www.genedenovo.com/article), and RNA purity and concentration were assessed using NanoDrop 2000 Spectrophotometer detection. The sequencing was performed on the Illumina HiseqTM 2500/4000 by Gene De novo Biotechnology. RNA differential expression analysis was performed using DESeq2 software between two different groups. The genes/transcripts with the parameter FDR < 0.05 and absolute fold change ≥ 2 were considered differentially expressed genes/transcripts. GO, KEGG, and GSEA analysis were performed using Omicsmart, a real-time interactive online platform for data analysis (http://www.omicsmart.com).

GO enrichment analysis provides all GO terms significantly enriched in DEGs compared with the genome background, and filters the DEGs that correspond to biological functions. First, all DEGs were

mapped to GO terms in the GO database, and gene numbers were calculated for every term. Significantly enriched GO terms in DEGs compared with the genome background were defined by hypergeometric test.

Pathway-based analysis helps to further understand genes' biological functions. KEGG is the major public pathway-related database. Pathway enrichment analysis identified significantly enriched metabolic pathways or signal transduction pathways in DEGs compared with the whole-genome background.

The treatments of mAb depletion

For the depletion of $CD8^+$ T cells, an anti-CD8α mAb (clone BE0117; BioXcell) was injected intraperitoneally starting at 5 days post high-titer AAV injection, with subsequent injections at days 10, 15, 20, and 25 (100 μg per mouse). At 30 dpi of AAV injection, immunohistochemistry (IHC) was carried out. To deplete the $CD4^+$ T cells, an anti-CD4 mAb (clone BE0003-3; BioXcell) was injected intraperitoneally starting at 5 days after high-titer AAV injection, with subsequent injections at days 10, 15, 20, and 25 (100 μg per mouse). IHC was carried out at 30 dpi of AAV injection. The isotype control was Rat IgG (clone BE0090; BioXcell), The administration time of the control group was consistent with the experimental group.

Neutralizing antibodies

The neutralizing antibodies of anti-GZMB mAb (clone sc-8022; Santa Cruz Biotechnology) were intracisternally injected (5 μL) starting at 10 days after high-titer AAV injection, then mice were repeatedly injected at 16 and 22 dpi (200 mg/mL, 5 μL per mouse). IHC was performed at 30 dpi of AAV injection. The isotype control was mouse IgG (clone sc-3837; Santa Cruz Biotechnology). The administration time of the control group was consistent with the experimental group.

Statistical analysis

The quantification data are expressed as mean ± SD from three to six mice. Statistical analysis was performed by the unpaired Student's t tests and one-way ANOVA analysis with the Tukey test. Differences were considered statistically significant at $p < 0.05$. Significant differences are indicated by $^*p < 0.05$, $^{**}p < 0.01$, $^{***}p < 0.001$, and $^{****}p < 0.0001$.

DATA AND CODE AVAILABILITY

The data that support the findings of this study are available from the corresponding author upon reasonable request.

SUPPLEMENTAL INFORMATION

Supplemental information can be found online at https://doi.org/10.1016/j.omtm.2023.08.021.

ACKNOWLEDGMENTS

This work was supported by the Jinan University Fund for Distinguished Young Scholars to Z.W., the Natural Science Foundation of Guangdong Province of China (no. 2022A1515012294 to Z.W.), Guangzhou Key Projects of Brain Science and Brain-Like Intelligence Technology (202206060002 to Z.W. and G.C.), and the Pearl River Innovation and Entrepreneurship Team (2021ZT09Y552 to Z.W. and G.C.).

AUTHOR CONTRIBUTIONS

Z.W. and G.C. supervised and designed the research. Y.-W.G., J.-L.C., W.-Y.J., L.X., Y.X., S.H., C.-Y.L., Z.-R.L., and K.-Y.H. performed all experiments. Y.-W.G., Z.W., and G.C. analyzed the data and made the figures. Y.-W.G. performed bioinformatics analysis. Y.-W.G., Z.W., and G.C. wrote the paper with input from all authors.

DECLARATION OF INTERESTS

G.C. is a co-founder of NeuExcell Therapeutics Inc.

REFERENCES

1. Kuzmin, D.A., Shutova, M.V., Johnston, N.R., Smith, O.P., Fedorin, V.V., Kukushkin, Y.S., van der Loo, J.C.M., and Johnstone, E.C. (2021). The clinical landscape for AAV gene therapies. Nat. Rev. Drug Discov. *20*, 173–174. https://doi.org/10.1038/d41573-021-00017-7.

2. Li, C., and Samulski, R.J. (2020). Engineering adeno-associated virus vectors for gene therapy. Nat. Rev. Genet. *21*, 255–272. https://doi.org/10.1038/s41576-019-0205-4.

3. Wang, D., Tai, P.W.L., and Gao, G. (2019). Adeno-associated virus vector as a platform for gene therapy delivery. Nat. Rev. Drug Discov. *18*, 358–378. https://doi.org/10.1038/s41573-019-0012-9.

4. Keiser, M.S., Ranum, P.T., Yrigollen, C.M., Carrell, E.M., Smith, G.R., Muehlmatt, A.L., Chen, Y.H., Stein, J.M., Wolf, R.L., Radaelli, E., et al. (2021). Toxicity after AAV delivery of RNAi expression constructs into nonhuman primate brain. Nat. Med. *27*, 1982–1989. https://doi.org/10.1038/s41591-021-01522-3.

5. Muhuri, M., Maeda, Y., Ma, H., Ram, S., Fitzgerald, K.A., Tai, P.W., and Gao, G. (2021). Overcoming innate immune barriers that impede AAV gene therapy vectors. J. Clin. Invest. *131*, e143780. https://doi.org/10.1172/JCI143780.

6. Van Alstyne, M., Tattoli, I., Delestrée, N., Recinos, Y., Workman, E., Shihabuddin, L.S., Zhang, C., Mentis, G.Z., and Pellizzoni, L. (2021). Gain of toxic function by long-term AAV9-mediated SMN overexpression in the sensorimotor circuit. Nat. Neurosci. *24*, 930–940. https://doi.org/10.1038/s41593-021-00827-3.

7. Ronzitti, G., Gross, D.A., and Mingozzi, F. (2020). Human Immune Responses to Adeno-Associated Virus (AAV) Vectors. Front. Immunol. *11*, 670. https://doi.org/10.3389/fimmu.2020.00670.

8. Shirley, J.L., de Jong, Y.P., Terhorst, C., and Herzog, R.W. (2020). Immune Responses to Viral Gene Therapy Vectors. Mol. Ther. *28*, 709–722. https://doi.org/10.1016/j.ymthe.2020.01.001.

9. Mingozzi, F., and High, K.A. (2017). Overcoming the Host Immune Response to Adeno-Associated Virus Gene Delivery Vectors: The Race Between Clearance, Tolerance, Neutralization, and Escape. Annu. Rev. Virol. *4*, 511–534. https://doi.org/10.1146/annurev-virology-101416-041936.

10. Chand, D., Mohr, F., McMillan, H., Tukov, F.F., Montgomery, K., Kleyn, A., Sun, R., Tauscher-Wisniewski, S., Kaufmann, P., and Kullak-Ublick, G. (2021). Hepatotoxicity following administration of onasemnogene abeparvovec (AVXS-101) for the treatment of spinal muscular atrophy. J. Hepatol. *74*, 560–566. https://doi.org/10.1016/j.jhep.2020.11.001.

11. Hinderer, C., Katz, N., Buza, E.L., Dyer, C., Goode, T., Bell, P., Richman, L.K., and Wilson, J.M. (2018). Severe Toxicity in Nonhuman Primates and Piglets Following High-Dose Intravenous Administration of an Adeno-Associated Virus Vector Expressing Human SMN. Hum. Gene Ther. *29*, 285–298. https://doi.org/10.1089/hum.2018.015.

12. Wilson, J.M., and Flotte, T.R. (2020). Moving Forward After Two Deaths in a Gene Therapy Trial of Myotubular Myopathy. Hum. Gene Ther. *31*, 695–696. https://doi.org/10.1089/hum.2020.182.

13. Hudry, E., and Vandenberghe, L.H. (2019). Therapeutic AAV Gene Transfer to the Nervous System: A Clinical Reality. Neuron *101*, 839–862. https://doi.org/10.1016/j.neuron.2019.02.017.

14. Sun, J., and Roy, S. (2021). Gene-based therapies for neurodegenerative diseases. Nat. Neurosci. *24*, 297–311. https://doi.org/10.1038/s41593-020-00778-1.

15. Yshii, L., Pasciuto, E., Bielefeld, P., Mascali, L., Lemaitre, P., Marino, M., Dooley, J., Kouser, L., Verschoren, S., Lagou, V., et al. (2022). Astrocyte-targeted gene delivery of interleukin 2 specifically increases brain-resident regulatory T cell numbers and protects against pathological neuroinflammation. Nat. Immunol. *23*, 878–891. https://doi.org/10.1038/s41590-022-01208-z.

16. Engelhardt, B., Vajkoczy, P., and Weller, R.O. (2017). The movers and shapers in immune privilege of the CNS. Nat. Immunol. *18*, 123–131. https://doi.org/10.1038/ni.3666.

17. Forrester, J.V., McMenamin, P.G., and Dando, S.J. (2018). CNS infection and immune privilege. Nat. Rev. Neurosci. *19*, 655–671. https://doi.org/10.1038/s41583-018-0070-8.

18. Abbott, N.J., Rönnbäck, L., and Hansson, E. (2006). Astrocyte-endothelial interactions at the blood-brain barrier. Nat. Rev. Neurosci. *7*, 41–53. https://doi.org/10.1038/nrn1824.

19. Chow, B.W., and Gu, C. (2015). The Molecular Constituents of the Blood-Brain Barrier. Trends Neurosci. *38*, 598–608. https://doi.org/10.1016/j.tins.2015.08.003.

20. Diaz-Castro, B., Robel, S., and Mishra, A. (2023). Astrocyte Endfeet in Brain Function and Pathology: Open Questions. Annu. Rev. Neurosci. https://doi.org/10.1146/annurev-neuro-091922-031205.

21. Sofroniew, M.V. (2015). Astrocyte barriers to neurotoxic inflammation. Nat. Rev. Neurosci. *16*, 249–263. https://doi.org/10.1038/nrn3898.

22. Obermeier, B., Daneman, R., and Ransohoff, R.M. (2013). Development, maintenance and disruption of the blood-brain barrier. Nat. Med. *19*, 1584–1596. https://doi.org/10.1038/nm.3407.

23. Sweeney, M.D., Sagare, A.P., and Zlokovic, B.V. (2018). Blood-brain barrier breakdown in Alzheimer disease and other neurodegenerative disorders. Nat. Rev. Neurol. *14*, 133–150. https://doi.org/10.1038/nrneurol.2017.188.

24. Zhao, Z., Nelson, A.R., Betsholtz, C., and Zlokovic, B.V. (2015). Establishment and Dysfunction of the Blood-Brain Barrier. Cell *163*, 1064–1078. https://doi.org/10.1016/j.cell.2015.10.067.

25. Leda, A.R., Bertrand, L., Andras, I.E., El-Hage, N., Nair, M., and Toborek, M. (2019). Selective Disruption of the Blood-Brain Barrier by Zika Virus. Front. Microbiol. *10*, 2158. https://doi.org/10.3389/fmicb.2019.02158.

26. Lee, M.H., Perl, D.P., Steiner, J., Pasternack, N., Li, W., Maric, D., Safavi, F., Horkayne-Szakaly, I., Jones, R., Stram, M.N., et al. (2022). Neurovascular injury with complement activation and inflammation in COVID-19. Brain *145*, 2555–2568. https://doi.org/10.1093/brain/awac151.

27. Spindler, K.R., and Hsu, T.H. (2012). Viral disruption of the blood brain barrier. Trends Microbiol. *20*, 282–290. https://doi.org/10.1016/j.tim.2012.03.009.

28. Wenzel, J., Lampe, J., Müller-Fielitz, H., Schuster, R., Zille, M., Müller, K., Krohn, M., Körbelin, J., Zhang, L., Özorhan, Ü., et al. (2021). The SARS-CoV-2 main protease M(pro) causes microvascular brain pathology by cleaving NEMO in brain endothelial cells. Nat. Neurosci. *24*, 1522–1533. https://doi.org/10.1038/s41593-021-00926-1.

29. Ortinski, P.I., Dong, J., Mungenast, A., Yue, C., Takano, H., Watson, D.J., Haydon, P.G., and Coulter, D.A. (2010). Selective induction of astrocytic gliosis generates deficits in neuronal inhibition. Nat. Neurosci. *13*, 584–591. https://doi.org/10.1038/nn.2535.

30. Griffin, J.M., Fackelmeier, B., Fong, D.M., Mouravlev, A., Young, D., and O'Carroll, S.J. (2019). Astrocyte-selective AAV gene therapy through the endogenous GFAP promoter results in robust transduction in the rat spinal cord following injury. Gene Ther. *26*, 198–210. https://doi.org/10.1038/s41434-019-0075-6.

31. Taschenberger, G., Tereshchenko, J., and Kügler, S. (2017). A MicroRNA124 Target Sequence Restores Astrocyte Specificity of gfaABC1D-Driven Transgene Expression in AAV-Mediated Gene Transfer. Mol. Ther. Nucleic Acids *8*, 13–25. https://doi.org/10.1016/j.omtn.2017.03.009.

32. Giehrl-Schwab, J., Giesert, F., Rauser, B., Lao, C.L., Hembach, S., Lefort, S., Ibarra, I.L., Koupourtidou, C., Luecken, M.D., Truong, D.J.J., et al. (2022). Parkinson's disease motor symptoms rescue by CRISPRa-reprogramming astrocytes into GABAergic neurons. EMBO Mol. Med. *14*, e14797. https://doi.org/10.15252/emmm.202114797.

33. Matsuda, T., Irie, T., Katsurabayashi, S., Hayashi, Y., Nagai, T., Hamazaki, N., Adefuin, A.M.D., Miura, F., Ito, T., Kimura, H., et al. (2019). Pioneer Factor NeuroD1 Rearranges Transcriptional and Epigenetic Profiles to Execute Microglia-Neuron Conversion. Neuron *101*, 472–485.e7. https://doi.org/10.1016/j.neuron.2018.12.010.

34. Wang, L.L., Serrano, C., Zhong, X., Ma, S., Zou, Y., and Zhang, C.L. (2021). Revisiting astrocyte to neuron conversion with lineage tracing *in vivo*. Cell *184*, 5465–5481.e16. https://doi.org/10.1016/j.cell.2021.09.005.

35. Zhou, H., Su, J., Hu, X., Zhou, C., Li, H., Chen, Z., Xiao, Q., Wang, B., Wu, W., Sun, Y., et al. (2020). Glia-to-Neuron Conversion by CRISPR-CasRx Alleviates Symptoms of Neurological Disease in Mice. Cell *181*, 590–603.e16. https://doi.org/10.1016/j.cell.2020.03.024.

36. Linnerbauer, M., Wheeler, M.A., and Quintana, F.J. (2020). Astrocyte Crosstalk in CNS Inflammation. Neuron *108*, 608–622. https://doi.org/10.1016/j.neuron.2020.08.012.

37. Terstappen, G.C., Meyer, A.H., Bell, R.D., and Zhang, W. (2021). Strategies for delivering therapeutics across the blood-brain barrier. Nat. Rev. Drug Discov. *20*, 362–383. https://doi.org/10.1038/s41573-021-00139-y.

38. Hinterleitner, C., Strähle, J., Malenke, E., Hinterleitner, M., Henning, M., Seehawer, M., Bilich, T., Heitmann, J., Lutz, M., Mattern, S., et al. (2021). Platelet PD-L1 reflects collective intratumoral PD-L1 expression and predicts immunotherapy response in non-small cell lung cancer. Nat. Commun. *12*, 7005. https://doi.org/10.1038/s41467-021-27303-7.

39. Hopperton, K.E., Mohammad, D., Trépanier, M.O., Giuliano, V., and Bazinet, R.P. (2018). Markers of microglia in post-mortem brain samples from patients with Alzheimer's disease: a systematic review. Mol. Psychiatr. *23*, 177–198. https://doi.org/10.1038/mp.2017.246.

40. Maecker, H.T., McCoy, J.P., and Nussenblatt, R. (2012). Standardizing immunophenotyping for the Human Immunology Project. Nat. Rev. Immunol. *12*, 191–200. https://doi.org/10.1038/nri3158.

41. Borodinova, A.A., Balaban, P.M., Bezprozvanny, I.B., Salmina, A.B., and Vlasova, O.L. (2021). Genetic Constructs for the Control of Astrocytes' Activity. Cells *10*, 1600. https://doi.org/10.3390/cells10071600.

42. Xiong, W., Wu, D.M., Xue, Y., Wang, S.K., Chung, M.J., Ji, X., Rana, P., Zhao, S.R., Mai, S., and Cepko, C.L. (2019). AAV cis-regulatory sequences are correlated with ocular toxicity. Proc. Natl. Acad. Sci. USA *116*, 5785–5794. https://doi.org/10.1073/pnas.1821000116.

43. Laidlaw, B.J., Craft, J.E., and Kaech, S.M. (2016). The multifaceted role of CD4(+) T cells in CD8(+) T cell memory. Nat. Rev. Immunol. *16*, 102–111. https://doi.org/10.1038/nri.2015.10.

44. Lee, H., Jeong, S., and Shin, E.C. (2022). Significance of bystander T cell activation in microbial infection. Nat. Immunol. *23*, 13–22. https://doi.org/10.1038/s41590-021-00985-3.

45. Neumann, H., Medana, I.M., Bauer, J., and Lassmann, H. (2002). Cytotoxic T lymphocytes in autoimmune and degenerative CNS diseases. Trends Neurosci. *25*, 313–319. https://doi.org/10.1016/S0166-2236(02)02154-9.

46. Swain, S.L., McKinstry, K.K., and Strutt, T.M. (2012). Expanding roles for CD4(+) T cells in immunity to viruses. Nat. Rev. Immunol. *12*, 136–148. https://doi.org/10.1038/nri3152.

47. Ansari, A.M., Ahmed, A.K., Matsangos, A.E., Lay, F., Born, L.J., Marti, G., Harmon, J.W., and Sun, Z. (2016). Cellular GFP Toxicity and Immunogenicity: Potential Confounders in in Vivo Cell Tracking Experiments. Stem Cell Rev. Rep. *12*, 553–559. https://doi.org/10.1007/s12015-016-9670-8.

48. Chan, Y.K., Wang, S.K., Chu, C.J., Copland, D.A., Letizia, A.J., Costa Verdera, H., Chiang, J.J., Sethi, M., Wang, M.K., Neidermyer, W.J., et al. (2021). Engineering adeno-associated viral vectors to evade innate immune and inflammatory responses. Sci. Transl. Med. *13*, abd3438. https://doi.org/10.1126/scitranslmed.

49. Faust, S.M., Bell, P., Cutler, B.J., Ashley, S.N., Zhu, Y., Rabinowitz, J.E., and Wilson, J.M. (2013). CpG-depleted adeno-associated virus vectors evade immune detection. J. Clin. Invest. *123*, 2994–3001. https://doi.org/10.1172/JCI68205.

50. Martino, A.T., Suzuki, M., Markusic, D.M., Zolotukhin, I., Ryals, R.C., Moghimi, B., Ertl, H.C.J., Muruve, D.A., Lee, B., and Herzog, R.W. (2011). The genome of self-complementary adeno-associated viral vectors increases Toll-like receptor 9-dependent innate immune responses in the liver. Blood *117*, 6459–6468. https://doi.org/10.1182/blood-2010-10-314518.

51. Daglas, M., Draxler, D.F., Ho, H., McCutcheon, F., Galle, A., Au, A.E., Larsson, P., Gregory, J., Alderuccio, F., Sashindranath, M., and Medcalf, R.L. (2019). Activated CD8(+) T Cells Cause Long-Term Neurological Impairment after Traumatic Brain Injury in Mice. Cell Rep. *29*, 1178–1191.e6. https://doi.org/10.1016/j.celrep.2019.09.046.

52. Frieser, D., Pignata, A., Khajavi, L., Shlesinger, D., Gonzalez-Fierro, C., Nguyen, X.H., Yermanos, A., Merkler, D., Höftberger, R., Desestret, V., et al. (2022). Tissue-resident CD8(+) T cells drive compartmentalized and chronic autoimmune damage against CNS neurons. Sci. Transl. Med. *14*, eabl6157. https://doi.org/10.1126/scitranslmed.abl6157.

53. Vincenti, I., Page, N., Steinbach, K., Yermanos, A., Lemeille, S., Nunez, N., Kreutzfeldt, M., Klimek, B., Di Liberto, G., Egervari, K., et al. (2022). Tissue-resident memory CD8(+) T cells cooperate with CD4(+) T cells to drive compartmentalized immunopathology in the CNS. Sci. Transl. Med. *14*, eabl6058. https://doi.org/10.1126/scitranslmed.abl6058.

54. Brioschi, S., Wang, W.L., Peng, V., Wang, M., Shchukina, I., Greenberg, Z.J., Bando, J.K., Jaeger, N., Czepielewski, R.S., Swain, A., et al. (2021). Heterogeneity of meningeal B cells reveals a lymphopoietic niche at the CNS borders. Science *373*. eabf9277–422. https://doi.org/10.1126/science.abf9277.

55. Cugurra, A., Mamuladze, T., Rustenhoven, J., Dykstra, T., Beroshvili, G., Greenberg, Z.J., Baker, W., Papadopoulos, Z., Drieu, A., Blackburn, S., et al. (2021). Skull and vertebral bone marrow are myeloid cell reservoirs for the meninges and CNS parenchyma. Science *373*, eabf7844. https://doi.org/10.1126/science.abf7844.

56. Mazzitelli, J.A., Smyth, L.C.D., Cross, K.A., Dykstra, T., Sun, J., Du, S., Mamuladze, T., Smirnov, I., Rustenhoven, J., and Kipnis, J. (2022). Cerebrospinal fluid regulates skull bone marrow niches via direct access through dural channels. Nat. Neurosci. *25*, 555–560. https://doi.org/10.1038/s41593-022-01029-1.

57. Rustenhoven, J., Drieu, A., Mamuladze, T., de Lima, K.A., Dykstra, T., Wall, M., Papadopoulos, Z., Kanamori, M., Salvador, A.F., Baker, W., et al. (2021). Functional characterization of the dural sinuses as a neuroimmune interface. Cell *184*, 1000–1016.e27. https://doi.org/10.1016/j.cell.2020.12.040.

58. Peters, C.W., Maguire, C.A., and Hanlon, K.S. (2021). Delivering AAV to the Central Nervous and Sensory Systems. Trends Pharmacol. Sci. *42*, 461–474. https://doi.org/10.1016/j.tips.2021.03.004.

59. Johnston, S., Parylak, S.L., Kim, S., Mac, N., Lim, C., Gallina, I., Bloyd, C., Newberry, A., Saavedra, C.D., Novak, O., et al. (2021). AAV ablates neurogenesis in the adult murine hippocampus. Elife *10*, e59291. https://doi.org/10.7554/eLife.59291.

60. Wang, T., Lee, M.H., Johnson, T., Allie, R., Hu, L., Calabresi, P.A., and Nath, A. (2010). Activated T-cells inhibit neurogenesis by releasing granzyme B: rescue by Kv1.3 blockers. J. Neurosci. *30*, 5020–5027. https://doi.org/10.1523/JNEUROSCI.0311-10.2010.

61. Albert, K., Voutilainen, M.H., Domanskyi, A., and Airavaara, M. (2017). AAV Vector-Mediated Gene Delivery to Substantia Nigra Dopamine Neurons: Implications for Gene Therapy and Disease Models. Genes *8*, 63. https://doi.org/10.3390/genes8020063.

62. Kim, C.K., Adhikari, A., and Deisseroth, K. (2017). Integration of optogenetics with complementary methodologies in systems neuroscience. Nat. Rev. Neurosci. *18*, 222–235. https://doi.org/10.1038/nrn.2017.15.

63. Nectow, A.R., and Nestler, E.J. (2020). Viral tools for neuroscience. Nat. Rev. Neurosci. *21*, 669–681. https://doi.org/10.1038/s41583-020-00382-z.

64. Chen, Y.C., Ma, N.X., Pei, Z.F., Wu, Z., Do-Monte, F.H., Keefe, S., Yellin, E., Chen, M.S., Yin, J.C., Lee, G., et al. (2020). A NeuroD1 AAV-Based Gene Therapy for Functional Brain Repair after Ischemic Injury through In Vivo Astrocyte-to-Neuron Conversion. Mol. Ther. *28*, 217–234. https://doi.org/10.1016/j.ymthe.2019.09.003.

65. Qian, H., and Fu, X.D. (2021). Brain Repair by Cell Replacement via In Situ Neuronal Reprogramming. Annu. Rev. Genet. *55*, 45–69. https://doi.org/10.1146/annurev-genet-071719-023616.

66. Wu, Z., Parry, M., Hou, X.Y., Liu, M.H., Wang, H., Cain, R., Pei, Z.F., Chen, Y.C., Guo, Z.Y., Abhijeet, S., and Chen, G. (2020). Gene therapy conversion of striatal astrocytes into GABAergic neurons in mouse models of Huntington's disease. Nat. Commun. *11*, 1105. https://doi.org/10.1038/s41467-020-14855-3.

67. Deverman, B.E., Ravina, B.M., Bankiewicz, K.S., Paul, S.M., and Sah, D.W.Y. (2018). Gene therapy for neurological disorders: progress and prospects. Nat. Rev. Drug Discov. *17*, 641–659. https://doi.org/10.1038/nrd.2018.110.

68. Leavitt, B.R., Kordasiewicz, H.B., and Schobel, S.A. (2020). Huntingtin-Lowering Therapies for Huntington Disease: A Review of the Evidence of Potential Benefits and Risks. JAMA Neurol. *77*, 764–772. https://doi.org/10.1001/jamaneurol.2020.0299.

69. Beckman, D., Chakrabarty, P., Ott, S., Dao, A., Zhou, E., Janssen, W.G., Donis-Cox, K., Muller, S., Kordower, J.H., and Morrison, J.H. (2021). A novel tau-based rhesus monkey model of Alzheimer's pathogenesis. Alzheimers Dement. *17*, 933–945. https://doi.org/10.1002/alz.12318.

70. Cook, C.N., Wu, Y., Odeh, H.M., Gendron, T.F., Jansen-West, K., del Rosso, G., Yue, M., Jiang, P., Gomes, E., Tong, J., et al. (2020). C9orf72 poly(GR) aggregation induces TDP-43 proteinopathy. Sci. Transl. Med. *12*, eabb3774. https://doi.org/10.1126/scitranslmed.abb3774.

71. Koprich, J.B., Kalia, L.V., and Brotchie, J.M. (2017). Animal models of alpha-synucleinopathy for Parkinson disease drug development. Nat. Rev. Neurosci. *18*, 515–529. https://doi.org/10.1038/nrn.2017.75.

72. Ravindra Kumar, S., Miles, T.F., Chen, X., Brown, D., Dobreva, T., Huang, Q., Ding, X., Luo, Y., Einarsson, P.H., Greenbaum, A., et al. (2020). Multiplexed Cre-dependent selection yields systemic AAVs for targeting distinct brain cell types. Nat. Methods *17*, 541–550. https://doi.org/10.1038/s41592-020-0799-7.

73. Goertsen, D., Flytzanis, N.C., Goeden, N., Chuapoco, M.R., Cummins, A., Chen, Y., Fan, Y., Zhang, Q., Sharma, J., Duan, Y., et al. (2022). AAV capsid variants with brain-wide transgene expression and decreased liver targeting after intravenous delivery in mouse and marmoset. Nat. Neurosci. *25*, 106–115. https://doi.org/10.1038/s41593-021-00969-4.

74. Lin, R., Zhou, Y., Yan, T., Wang, R., Li, H., Wu, Z., Zhang, X., Zhou, X., Zhao, F., Zhang, L., et al. (2022). Directed evolution of adeno-associated virus for efficient gene delivery to microglia. Nat. Methods *19*, 976–985. https://doi.org/10.1038/s41592-022-01547-7.

75. Chan, K.Y., Jang, M.J., Yoo, B.B., Greenbaum, A., Ravi, N., Wu, W.L., Sánchez-Guardado, L., Lois, C., Mazmanian, S.K., Deverman, B.E., and Gradinaru, V. (2017). Engineered AAVs for efficient noninvasive gene delivery to the central and peripheral nervous systems. Nat. Neurosci. *20*, 1172–1179. https://doi.org/10.1038/nn.4593.

76. Deverman, B.E., Pravdo, P.L., Simpson, B.P., Kumar, S.R., Chan, K.Y., Banerjee, A., Wu, W.L., Yang, B., Huber, N., Pasca, S.P., and Gradinaru, V. (2016). Cre-dependent selection yields AAV variants for widespread gene transfer to the adult brain. Nat. Biotechnol. *34*, 204–209. https://doi.org/10.1038/nbt.3440.

OMTM, Volume *31*

Supplemental information

High-titer AAV disrupts cerebrovascular integrity and induces lymphocyte infiltration in adult mouse brain

Yaowei Guo, Junliang Chen, Wenyu Ji, Liang Xu, Yu Xie, Shu He, Chuying Lai, Kaiyu Hou, Zeru Li, Gong Chen, and Zheng Wu

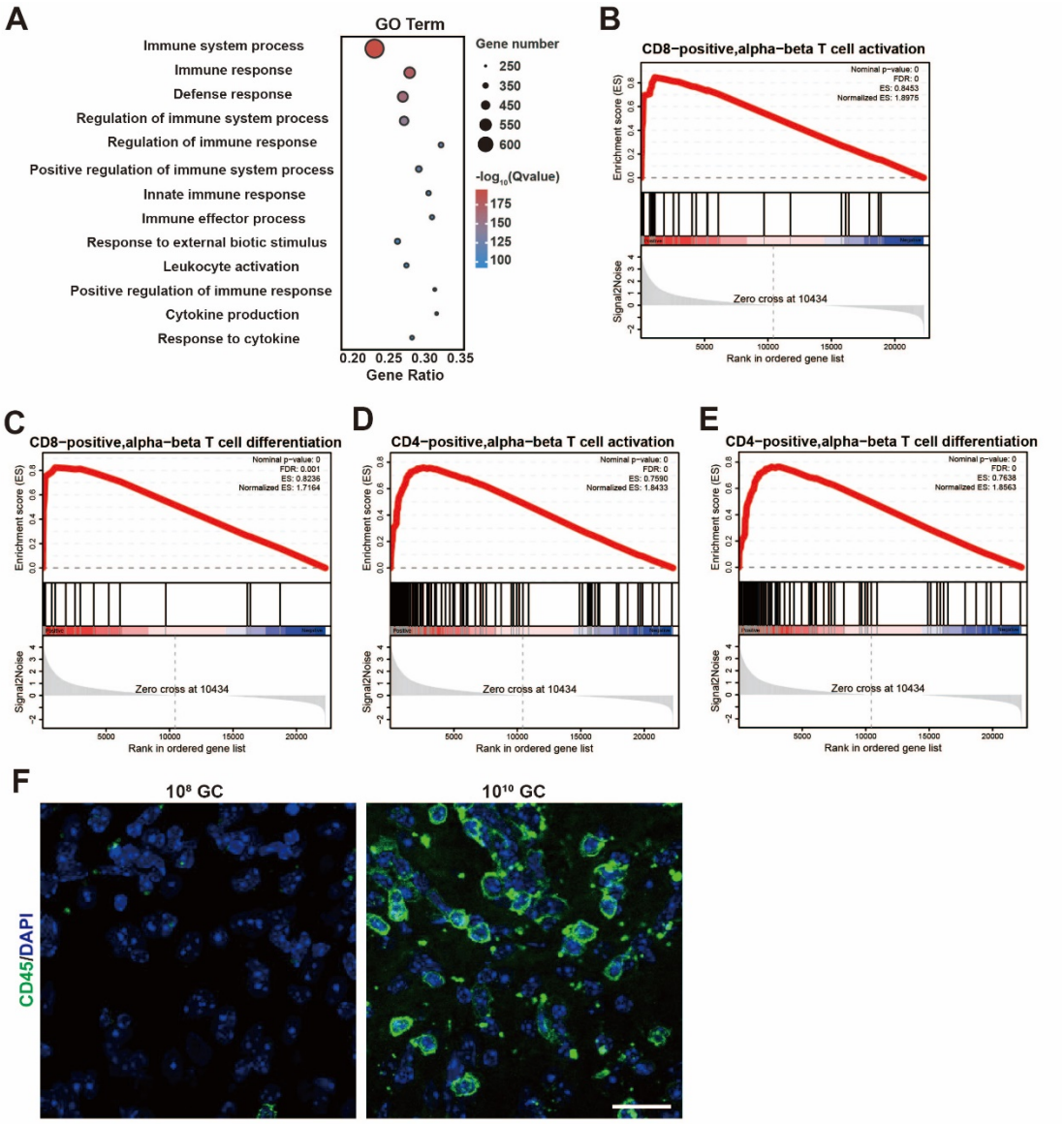

Figure S1. The GO term and GSEA (Gene Set Enrichment Analysis) analysis of bulk RNA-seq. (A) Go-enriched bubble plots showing that high doses of virus induce strong immune responses in mouse brains. (B) GSEA analysis of CD8-positive alpha-beta T cell activation. (C) GSEA analysis of CD8-positive alpha-beta T cell differentiation. (D) GSEA analysis of CD4-positive alpha-beta T cell activation. (E) GSEA analysis of CD4-positive alpha-beta T cell differentiation. (F) Confocal imaging of CD45 (green, leukocyte marker) at 30 dpi. Note that many $CD45^{+}$ leukocytes were detected in the brain parenchyma after high-titer AAV injection. Scale bar = 20 μm.

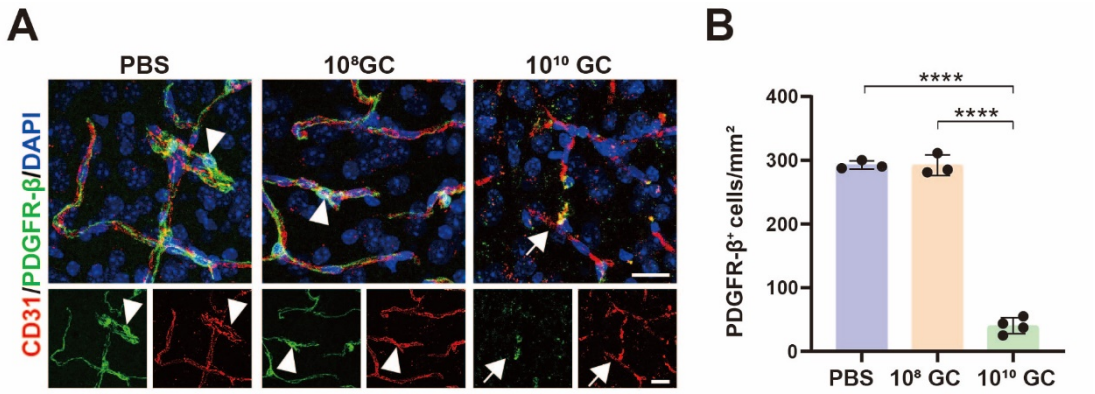

Figure S2. High-titer AAVs result in pericyte injury. (A) Confocal imaging of CD31 (red, endothelial cell marker) co-stained with PDGFR-β (green, pericyte marker) at 30 dpi. In PBS and 10^8 GC groups, many pericytes were associated with endothelial cells ($CD31^+$, indicated by arrowheads), however, pericytes were significantly damaged and endothelial cells lost pericyte sheath (indicated by arrows) in 10^{10} GC group. Scale bar = 20 μm. (B) Quantifications of PDGFR-β^+ cell numbers in PBS, 10^8 GC and 10^{10} GC groups. Values are shown as mean ± SD. n = 3-4 mice per group. One-way ANOVA analysis with Tukey test. Significance reported as ****$p < 0.0001$.

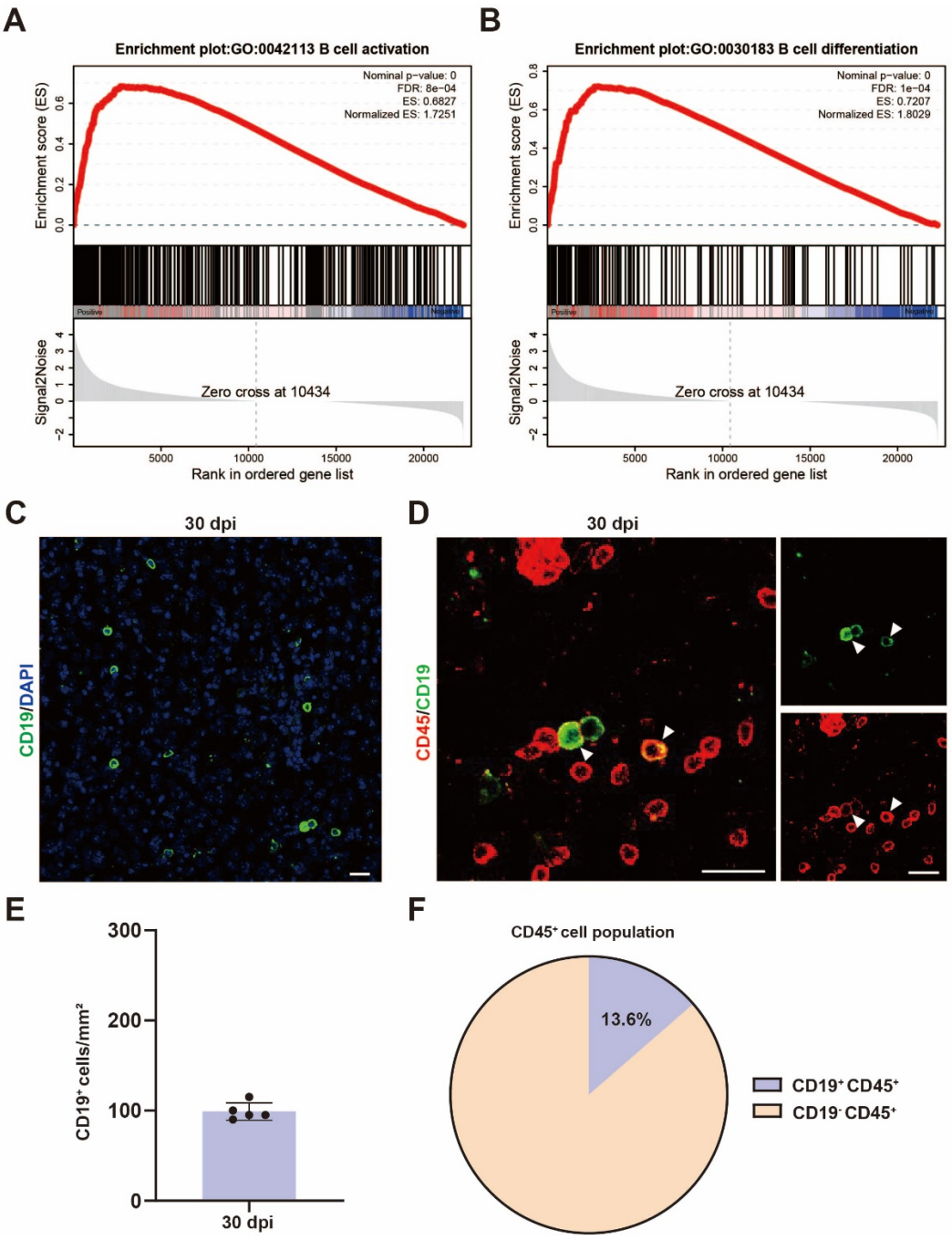

Figure S3. High-titer AAVs cause B cell infiltration. (A, B) GSEA analysis of B cell activation (A) and differentiation (B). (C) CD19 immunostaining (B cell marker) in the cortex at 30 days post high-titer AAV injection. Scale bar = 20 μm. (D) Confocal imaging of CD45 (red) co-stained with CD19 (green) at 30 dpi. CD19-positive cells were well co-labeled with CD45 (indicated by arrowheads). Scale bar = 20 μm. (E) Quantification of $CD19^+$ cell numbers at 30 dpi. (F) The pie chart showing that 13.6% of $CD45^+$ cells are CD19 positive.

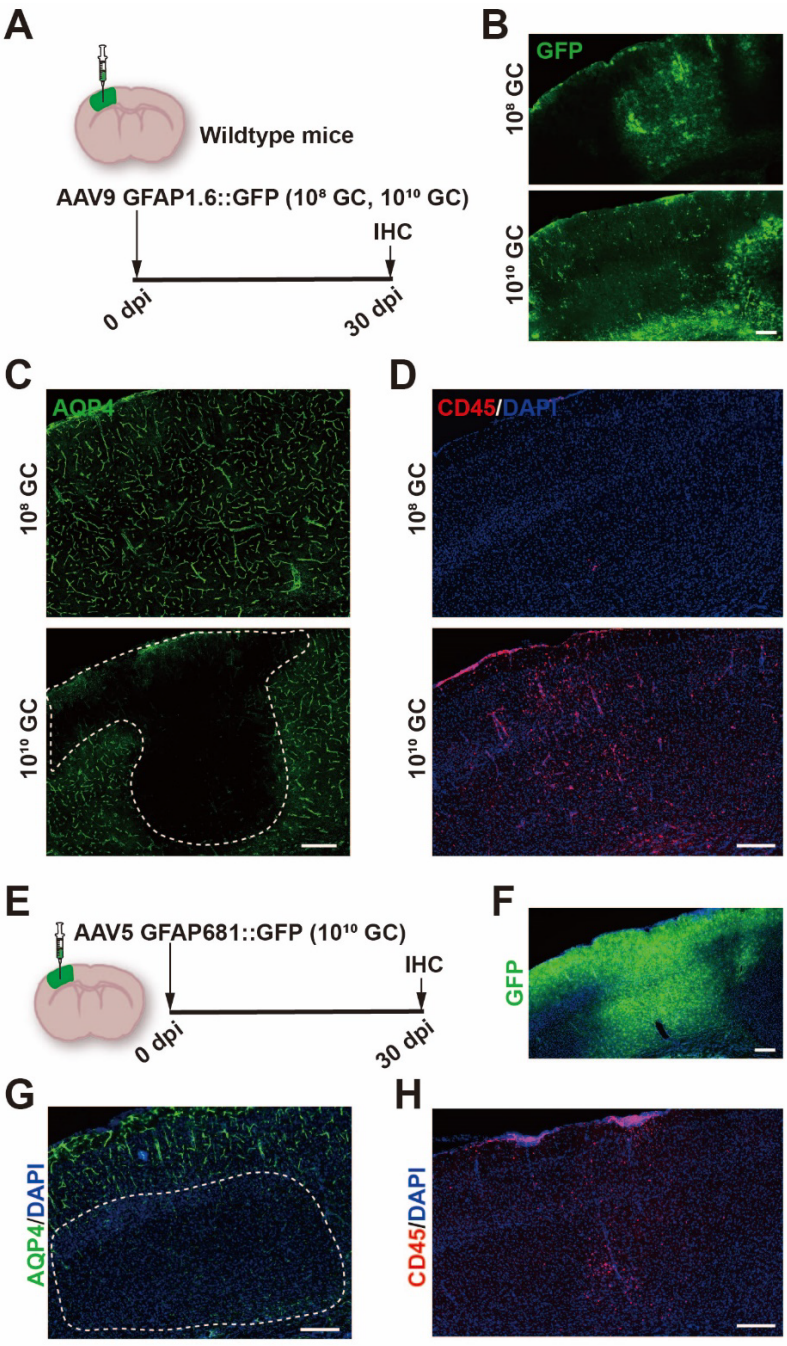

Figure S4. Different subtypes of GFAP promoters also cause immune cell infiltration. (A) Experimental design of GFAP1.6 promoter. (B) GFP expression in 10^8 GC and 10^{10} GC groups at 30 dpi. Scale bar = 200 μm. (C) AQP4 (green) signals were lost in high-titer AAV9 injected area (bottom, white dashed box) compare to low-titer AAV9 treated mice (top). Scale bar = 200 μm. (D) CD45 positive immune cells infiltrated the cortex of mice in 10^{10} GC group. Scale bar = 200 μm. (E) Experimental design of GFAP681 promoter. (F) GFP expression in 10^{10} GC group at 30 dpi. Scale bar = 200 μm. (G) AQP4 (green) signals were lost in the area of injecting with 10^{10} GC AAV5 (white dashed box). Scale bar = 200 μm. (H) The mouse cortex was infiltrated by CD45-positive cells in 10^{10} GC group. Scale bar = 200 μm.

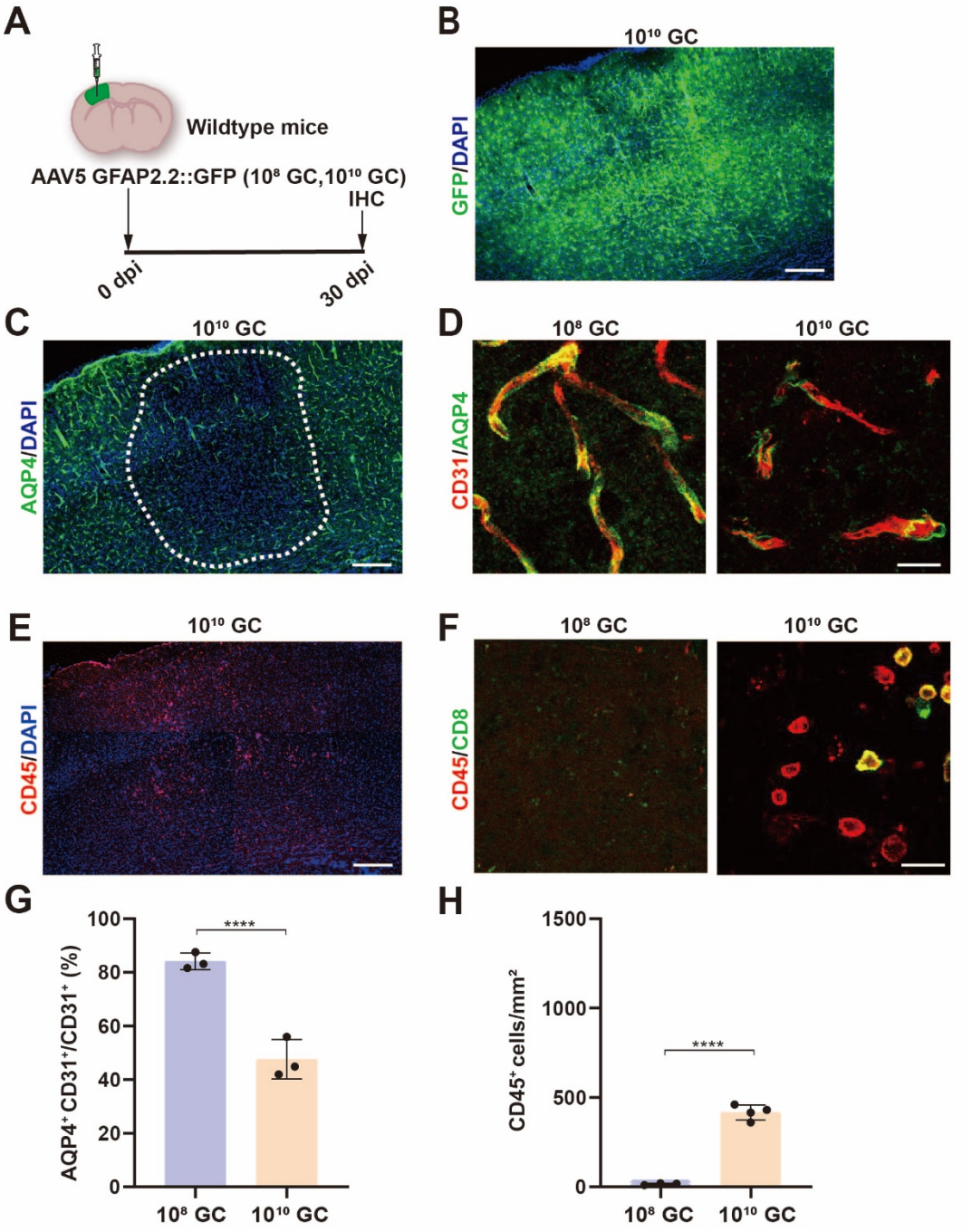

Figure S5. High-titer AAV5 also results in BBB disruption and leukocyte infiltration. (A) Experimental design of AAV5 intracranial injection study. (B) GFP expression in the cortex at 30 dpi. Scale bar = 200 μm. (C) AQP4 signals were lost in the high-titer AAV5 infected brain regions (white dashed box). Scale bar = 200 μm. (D) High-magnification images of CD31 (red) co-stained with AQP4 (green) in low-titer (left) and high-titer AAV5 (right) treated mice at 30 dpi. Scale bar = 20 μm. (E) Low-magnification images of CD45 immunostaining (red) in high-titer AAV5 treated mouse brain at 30 dpi. Scale bar = 200 μm. (F) High-magnification images of CD45 (red) co-stained with CD8 (green) in low-titer (left) and high-titer AAV5 (right) treated mice at 30 dpi. Scale bar = 20 μm. (G) Quantified data showing the ratio of total $AQP4^+$ signals

to total CD31$^+$ signals at 30 dpi. (H) Quantifications of CD45$^+$ cell density at 30 dpi. Values are shown as mean ± SD. n = 3-4 mice per group. Two-tailed Student's t-test. Significance reported as ****p < 0.0001.

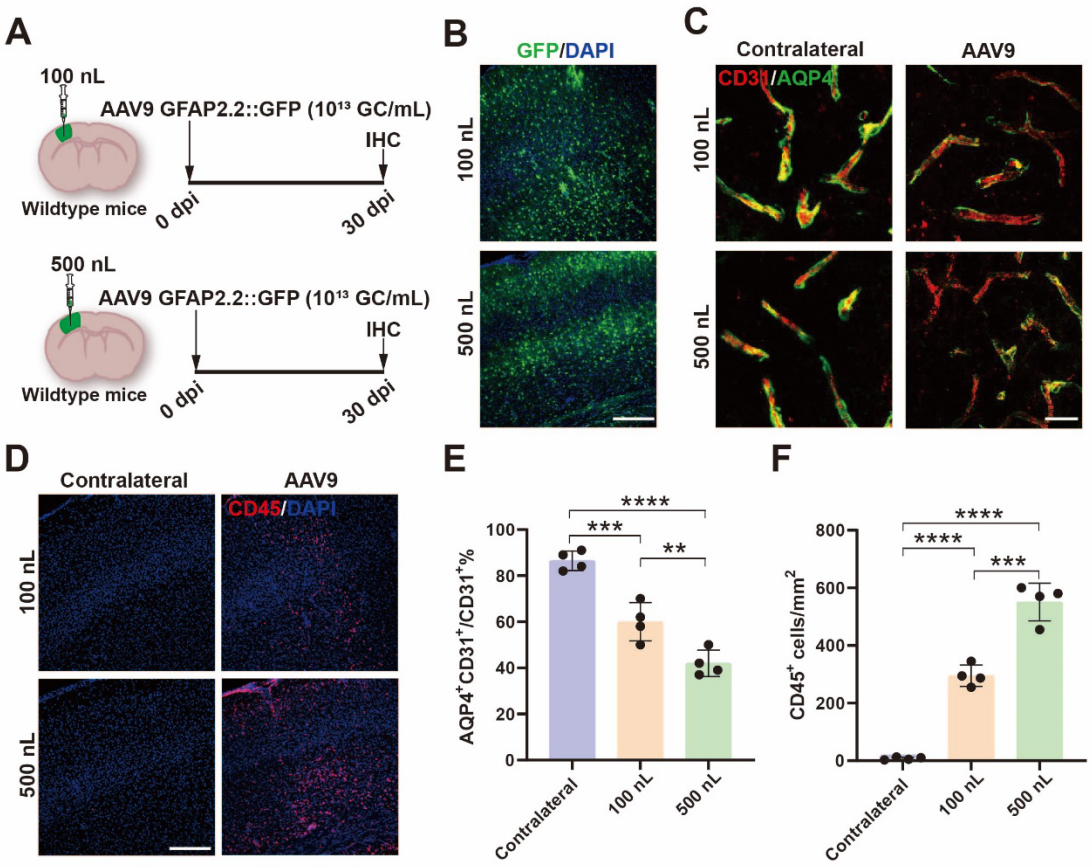

Figure S6. High-titer AAVs cause BBB disruption and leukocyte infiltration under injection volume below 1 µL conditions. (A) AAV injected area, volume, serotype and experimental timeline. (B) GFP expression in the cortex after injection of 100 nL (top) and 500 nL (bottom) AAV9. Scale bar = 200 µm. (C) Decreased AQP4 was detected perivascularly in both 100 nL and 500 nL injected mice compared to the contralateral side. Scale bar = 20 µm. (D) Leukocyte infiltration was also presented in both 100 nL and 500 nL injected areas. Scale bar = 200 µm. (E) Quantified data showing the percentage of cerebral blood vessels with AQP4 sheath at 30 dpi. (F) Quantifications of CD45$^+$ cell density at 30 dpi. Values are shown as mean ± SD. n = 4 mice per group. One-way ANOVA analysis with Tukey test. Significance reported as **p < 0.01, ***p < 0.001. ****p < 0.0001.

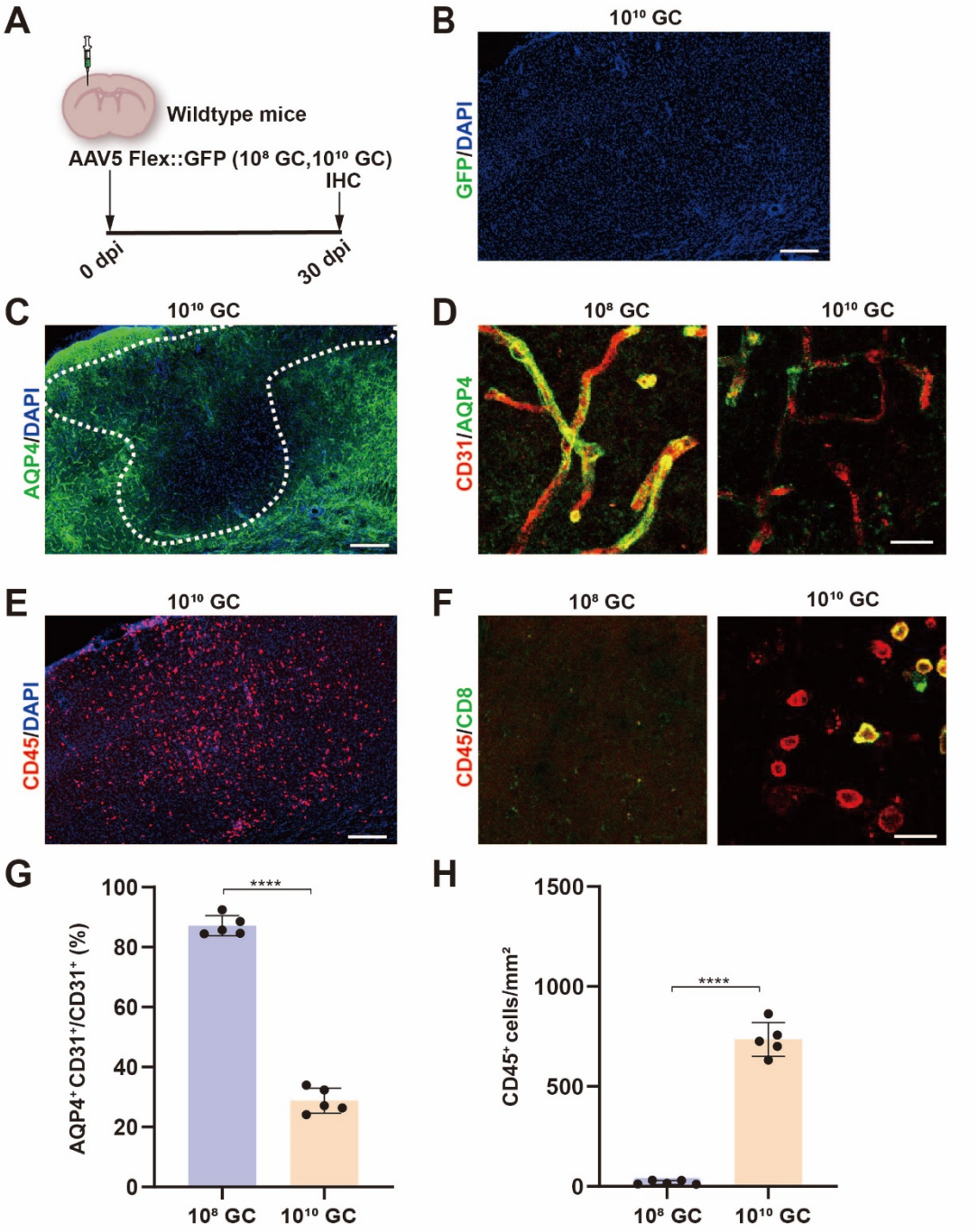

Figure S7. High-titer AAV5 induced BBB breakdown and leukocyte infiltration also independent of GFP expression. (A) Experimental design. AAV5-CAG::Flex-GFP was injected in wild-type mouse cortex. (B) No GFP expression in wild-type mouse brain after injection of AAV5-CAG::Flex-GFP. Scale bar = 200 μm. (C) AQP4 signals were lost at the site of AAV5 injected area (white dashed box). Scale bar = 200 μm. (D) Confocal imaging of CD31 (red) co-stained with AQP4 (green) in low-titer (left) and high-titer AAV5 (right) treated mice at 30 dpi. Scale bar = 20 μm. (E) CD45 positive leukocytes were invaded into the mouse brain parenchyma after high-titer AAV5 injection. Scale bar = 200 μm. (F) Confocal imaging of CD45 (red) co-stained with CD8 (green) in low-titer (left) and high-titer AAV5 (right) treated mice at 30 dpi.

Scale bar = 20 μm. (G) Quantification data showing that perivascular astrocytic endfeet were significantly reduced after injection of high-titer AAV5 at 30 dpi. (H) Quantitative data showing significant leukocyte invasion in high-titer AAV5 treated group. Values are shown as mean ± SD. n = 5 mice per group. Two-tailed Student's t-test. Significance reported as ****p < 0.0001.

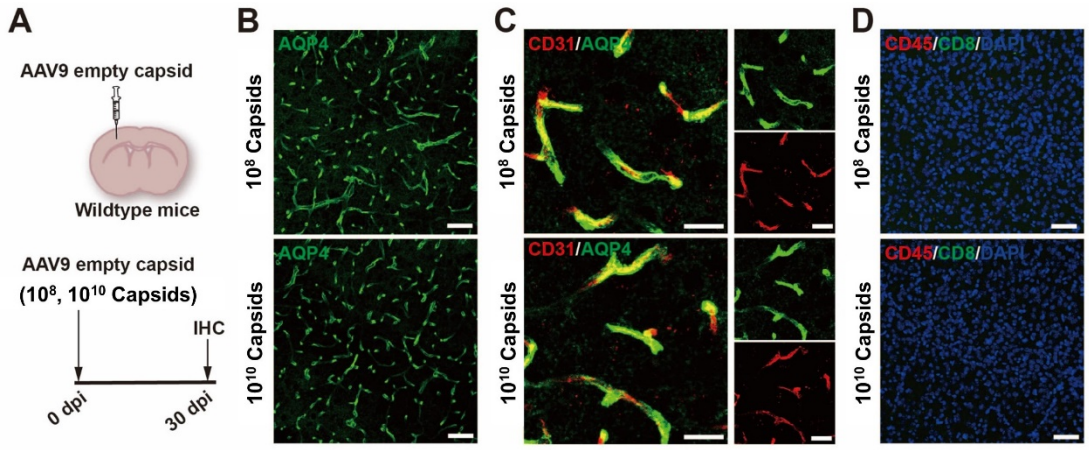

Figure S8. Injection of empty AAV9 viral capsids did not induce BBB disruption and leukocyte invasion in brain parenchyma. (A) Experimental design. (B) Low magnification confocal images of immunostaining for the astrocytic endfoot marker AQP4 surrounding the injection site of empty viral capsid. Note that neither low titer (top) nor high titer (bottom) empty capsids caused any apparent loss of AQP4 signal (n = 5 mice per group). Scale bar = 50 μm. (C) High magnification confocal images of CD31 (red) and AQP4 (green) co-immunostaining. The fluorescent signal of CD31 is perfectly encapsulated by AQP4, which is observed in both low-titer (top) and high-titer (bottom) empty viral capsid treated mice. Scale bar = 20 μm. (D) Leukocyte infiltration was not detected after AAV9 empty capsid injection (n = 5 mice per group). Scale bar = 50 μm.

Table S1. AAV information

Virus	Promoter and length	Volume	Original titer
AAV9 GFAP2.2::GFP	GFAP2.2 (2210 bp)	0.1-1 μL	2.30 x 10^{13} GC/mL
AAV9 GFAP1.6::GFP	GFAP1.6 (1677 bp)	1 μL	7.70 x 10^{13} GC/mL
AAV5 GFAP2.2::GFP	GFAP2.2 (2210 bp)	1 μL	2.50 x 10^{13} GC/mL
AAV5 GFAP681::GFP	GFAP681 (681 bp)	1 μL	3.47 x 10^{13} GC/mL
AAV9 FLEX::GFP	CAG (868 bp)	1 μL	6.09 x 10^{13} GC/mL
AAV5 FLEX::GFP	CAG (868 bp)	1 μL	8.34 x 10^{13} GC/mL
AAV9 empty capsid	None	1 μL	1.56 x 10^{14} Capsids/mL

Table S2. Primary antibody information

Antibodies(dilution)	Host	Source	Catalog#
AQP4 (1:1000)	Rabbit	Proteintech	16473-1-AP
CD31 (1:300)	Rat	BD Bioscience	550274
CD45 (1:500)	Rat	BD Bioscience	550539
CD45 (1:500)	Rabbit	Cell Signaling	70257
CD4 (1:500)	Rat	ThermoFisher	14-0042-82
CD68 (1:1000)	Rabbit	Abcam	Ab125212
CD8α (1:1000)	Rabbit	Abcam	Ab217334
GFAP (1:1000)	Rat	Invitrogen	13-0300
GFAP (1:1000)	Rabbit	DAKO	Z0334
Iba1 (1:1000)	Rabbit	Wako	019-19741
ZO-1 (1:300)	Rat	DSHB	R26.4C
Occludin (1:300)	Mouse	Santa Cruz Biotechnology	sc-133256
CD41 (1:1000)	Rat	Abcam	Ab33661
CD31 (1:300)	Rabbit	Abcam	Ab28364
CD19 (1:500)	Mouse	Santa Cruz Biotechnology	sc-373897
NeuN (1:2000)	Guinea pig	Millipore	ABN90
GFP (1:2000)	Chicken	Abcam	Ab13970
Granzyme B (1:2000)	Mouse	Santa Cruz Biotechnology	sc-8022